Title	Tissue characerisation of lung fibrosis: assessment with late-enhancement magnetic resonance imaging
Authors(s)	Brady, Darragh
Publication date	2015
Publisher	University College Dublin. School of Medicine and Medical Science
Link to online version	http://dissertations.umi.com/ucd:10040
Item record/more information	http://hdl.handle.net/10197/6810

TISSUE CHARACTERISATION OF LUNG FIBROSIS: Assessment with Late-Enhancement Magnetic Resonance Imaging

1 Volume
Darragh Brady MB BAO BCh MRCPI
Student Number: 96523760

The thesis is submitted to University College Dublin for the degree of Doctor of Medicine

Date of Submission: April 2015

School of Medicine and Health Sciences

Head of School: Professor Patrick Murray

Principal Supervisor: Professor Jonathan Dodd

Declaration

I hereby certify that the submitted work is my own work, was completed while registered as a candidate for the degree of doctor of medicine in imaging, and I have not obtained a degree elsewhere on the basis of the research presented in this submitted work.

Where information has been derived from other sources, I confirm that this has been indicated in the thesis.

I have collaborated with Professor Jonathan Dodd principally during this study. His help was intrinsic to conception of the project, and to manuscript editing. Dr Lisa Lavelle was also intrinsic to patient recruitment.

Contents

List of Tables

List of Figures

Abstract

Accurate depiction and quantification of lung fibrosis is important for diagnosis, treatment and prognosis of conditions that cause loss of function by fibrotic pulmonary process.

The gold-standard non-invasive imaging test of pulmonary fibrosis remains chest computed tomography (CT), which relies on the anatomical depiction of fibrosis, characterised by increased septal lines, traction bronchiectasis and honeycombing as the hallmarks of pulmonary fibrosis.

Magnetic resonance (MR), has the potential to characterise different tissues, based on composition and relaxation parameters, without the drawback of ionizing radiation. This ability to differentiate based on tissue type represents a different paradigm of pulmonary fibrosis imaging, based on a tissue characterization model rather than a purely anatomical one.

Late gadolinium enhancement (LE) has been used in cardiac MR imaging to detect and quantify myocardial fibrosis, whose enlarged extracellular space provides a nidus for gadolinium to concentrate and thus produce a signal on T1 based imaging.

We hypothesize that the same rationale will allow depiction of lung fibrosis given its tissue histopathological characteristics, and the studies that follow will test this hypothesis in two conditions with this pathological substrate, idiopathic pulmonary fibrosis and pulmonary sarcoidosis.

If we can depict pulmonary fibrosis using this MR sequence, it would represent a major advance in the imaging of lung fibrosis in sarcoidosis and idiopathic pulmonary fibrosis (IPF), and open up the door to the possibility of specific contrast

imaging markers linked to gadolinium that might bind to fibrotic receptors, thus increasing the specificity of imaging in these disorders.

Acknowledgements

Jonathan Dodd, MB MSc, Professor of Radiology, St. Vincent's Hospital, Dublin

Lisa Lavelle, MB, Department of Radiology, St. Vincent's Hospital, Dublin

Sinead McEvoy, MB, Department of Radiology, St. Vincent's Hospital, Dublin

David Murphy, MB, Department of Radiology, St. Vincent's Hospital, Dublin

Annika Gallagher, Department of Radiology, St. Vincent's Hospital, Dublin

Brian Gibney, MB, Department of Radiology, St. Vincent's Hospital, Dublin

Fionnula Shortt, BSc, Department of Radiology, St. Vincent's Hospital, Dublin

Marie McMullen, BSc, Department of Radiology, St. Vincent's Hospital, Dublin

Aurelie Fabry, MB PhD, Consultant Histopathologist, St. Vincent's Hospital, Dublin

Seamus Donnelly, MB MD, Professor of Medicine, St. Vincent's Hospital, Dublin

Madeline Martinez, New York City, NY

1 Introduction

1.1 Background

The origins of magnetic resonance imaging are based on the work of many individuals, [Ramsey, 1999] though the phenomenon of nuclear magnetic resonance is initially traceable to Rabi et al. [Rabi, 1938]

The idea of tissue characterization traces to Raymond Damadian who used spin echo nuclear magnetic resonance measurements. He noted differing relaxation times between benign and malignant tissues in rat specimens, and concluded that such methods could be used to distinguish tissue types. [Damadian, 1971]

However it was Paul Laterbur's idea of applying field gradients in all three dimensions, allowing a method for spatial localisation, that proved the key to functional imaging. He called his technique zeugmatography, a name that was later replaced by magnetic resonance imaging. [Laterbur, 1973; Laterbur, 1974]

Kumar et. al refined his reconstruction method of backprojection, by using the mathematical process of Fourier transformation, to describe an effective technique for the formation of two and three dimensional images. [Kumar, 1975]

In the years since, the manipulation of magnetic resonance as an imaging modality has had a consistent upwards trajectory. The facets that make it particularly advantageous are several fold. It allows the visualisation of protonic physics in vivo. Proton density, and magnetic effects on proton relaxation can be used to reflect

morphological information, providing excellent soft-tissue resolution and discrimination in arbitrary imaging planes. [Liszewski, 2013; Biederer, 2014] Molecules in motion can be imaged to provide physiological information, including perfusion [Bauman, 2014], oxygen levels within the alveoli, [Kadlecek, 2013] biochemical composition, [Kauppinen, 2011] biomechanical properties, [McGee, 2012] and the diffusion of tissue water, [Coolen, 2014] among others.

Magnetic resonance does all of this using non-ionising radiation. In many tissues it has demonstrated superiority or equivalence over conventional computed tomographic methods. However, despite the advances in technology, clinical imaging of lung tissue has proven challenging, and further advancements are needed.

The aim of this work has been to advance another method of imaging fibrotic lung tissue in vivo, based on delayed enhancement techniques.

1.2 Outline

This thesis focuses on an in vivo technique to image fibrosis in lung tissue. The studies included are feasability, prospective studies on patients with two distinct conditions that result in lung fibrosis.

Chapter one presents a background to magnetic resonance (MR), its historical origins, its role in modern imaging, and an outline of the thesis.

Chapter two presents the basics of magnetic resonance and how it is applied as an imaging technique. The concepts necessary to understand magnetic resonance imaging are presented briefly; how an image is formed and an explanation of the basic sequences. This chapter acts as a primer for the subsequent studies with an explanation of the key sequences used.

Chapter three focuses on thoracic imaging with MR; the specific dilemmas faced in relation to imaging lung tissue, and some potential solutions; and the modern application of MR to pulmonary disease, and its clinical utility.

Chapter four presents the condition of sarcoidosis. Its biology, pathophysiology, clinical manifestations and potential treatments are discussed. A review of the current radiological methods for sarcoidosis detection and staging is presented.

Chapter five introduces the background to our study. There is a discussion on the theoretical basis of late enhancement, and a rationale is presented for the use of this method to image lung fibrosis. The patient population, materials and methods of the study is described, and results are presented. A discussion on the findings describes the application of this new sequence in imaging lung fibrosis in sarcoidosis and the implications of this study for future research.

Chapter six presents the etiology, immunopathogenesis and clinical manifestations of idiopathic pulmonary fibrosis. Diagnostic criteria are discussed, and the role of imaging is presented.

Chapter seven focuses on the application of MR in the imaging of idiopathic pulmonary fibrosis, and presents the rationale for the use of a late enhancement sequence for depiction of lung fibrosis in this disease. The patient population, materials and methods of the study is described, and results are presented. A discussion on the findings describes the application of this new sequence in imaging lung fibrosis in idiopathic pulmonary fibrosis and the implications of this study for future research.

Chapter eight summarizes the findings of the studies, and its contribution to the sum of knowledge in lung imaging of these and other fibrotic lung conditions.

2 The basics of magnetic resonance imaging

2.1 MR Physics

This section deals with the basic physics of magnetic resonance.

2.1.1 Spin

Spin is the essential property of magnetic resonance.

The subatomic particles that make up the nucleus, protons and neutrons, possess this property of spin or angular momentum. They may spin in opposite directions, and when of even number, their net effect is spin cancellation. [Hanson, 2008]

Thus only nucleii with an uneven number of nucleons will possess net angular momentum. [Plewes, 2012]

Although spin requires a quantum cause, the rest of this explanation will defer to classical physical description. [Brown, 2003]

2.1.2 Polarisation

If protons, which are charged, have spin, then they will also have an associated magnetic field or moment.

Thus nuclei with spin behave as misincule magnets, which, when placed in an external magnetic field, are subject to a torque and will have a general tendency to align with the field. [Pooley, 2005]

The net magnetization, denoted M_0 at equilibrium, is a vectoral summation of the individual magnetic moments. The direction of M_0 defines the z-axis, and magnetisation parallel to this is called longitudinal magnetization. This z-axis component is the magnetization available for signal generation. [Markl, 2012]

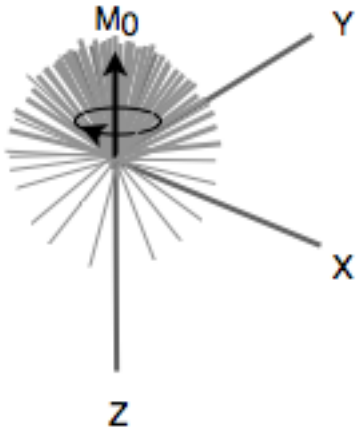

Fig 1: The distribution of many magnetic vector (gray) summate to a net magnetic vector, M_0 (black), which precesses about the z-axis with rotational frequency, ω_0.

2.1.3 Precession

The nucleus will continue to spin, however the influence of the torque of the external magnetic field (B_0) will push it into alignment.

The competing influences cause a helical rotation of the nucleus within B_0. This helical trajectory about the axis of B_0 is called precession.

The frequency of this precession is proportion to the torque of the external magnetic field. [Hornak, 2014]

2.1.4 Larmor frequency

The relationship between the torque of the external magnetic field, and the frequency of precession about the axis of B_0 is given by the equation;

$$\omega_0 = \gamma B_0$$

and is called the Larmor frequency (ω_0), named after Joseph Larmor, 1857-1942, an Irish physicist. The proportionality constant γ is the gyromagnetic ratio, and is specific to each nucleus. [Paschal, 2004]

2.1.5 Resonance

The condition of resonance occurs when the Larmor frequency of the precessing nucleus is matched by a magnetic field of the same frequency. [Bloch, 1946; Purcell, 1946]

A group of nuclei whose net magnetic moment is parallel to B_0, when a second magnetic field, denoted B_1, of the same frequency (on-resonance) in an orthogonal axis is introduced, experience an additional torque that pushes the net magnetic moment off axis of B_0.

B_1, the second magnetic field is referred to as an RF pulse as the resonance frequency of nuclei is in the radiofrequency range. It is a time varying field induced by an alternating current of the Larmor frequency.

Its effect is described as a flip, whose angle (α) can be quantified.

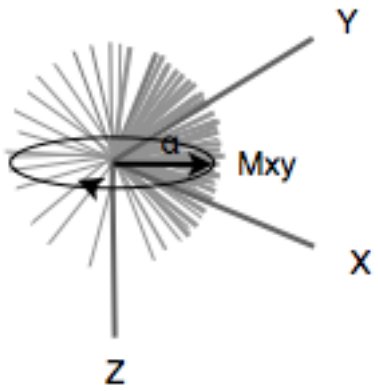

Fig 2: The net magnetic vector, is flipped into the xy-axis by a flip angle, α, and still rotates about the z-axis with with rotational frequency, ω_0.

2.1.6 Signal

If B_1 is turned on for a sufficient time (t) to induce a flip angle of 90° in the net magnetic moment (M_0), its rotating magnetic field can induce a current flow in a coil placed near it, as described by Faraday's laws.

This current is proportional to the magnitude of the magnetisation, which is a measure of the number of spins, or proton density, in the resonating tissue.

The kinetics of the induced signal show an initial maximum, followed by an exponential decay, as the RF pulse is turned off and the net magnetic moment returns to a position parallel to B_0. [Hornak, 2014]

This signal is called the free induction decay current. It will persist as long as M_{xy} has a non-zero component. [Markl, 2012]

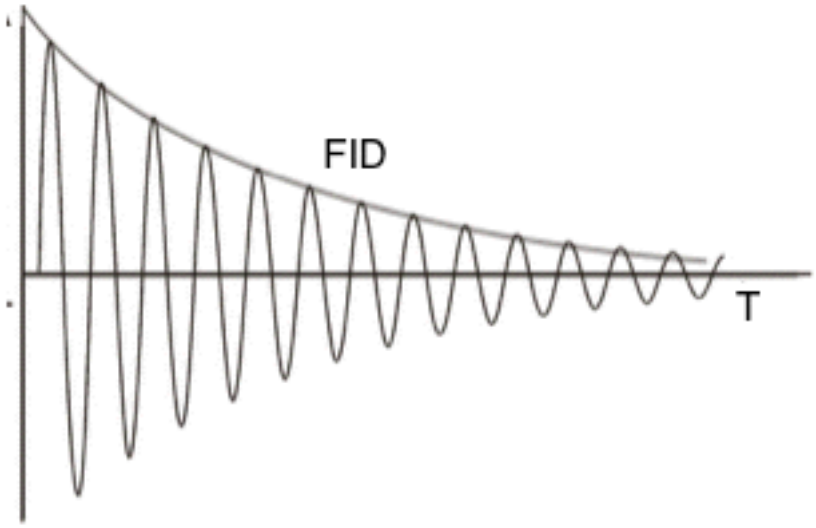

Fig 3: The free induced current amplitude decays with time (FID).

2.1.7 Relaxation

The RF excitation will flip the longitudinal magnetisation into the transverse xy plane, though the individual vectors will continue to precess about the z axis.

Nuclei that have been flipped will, when B_1 is turned off, return to precess about B_0. This process is called relaxation.

The net magnetic moment, when parallel to B_0 has no perpendicular component, and when flipped, can be resolved into parallel and perpendicular components. [Haacke, 1999]

T_1 is a time constant used to describe the relaxation of the parallel component and T_2 describes the relaxation of the perpendicular component.

Spin relaxation is caused by energy exchange.

T_2 relaxation is due to an exchange of energy between adjacent spins, leading to inhomogeneities in B_0 and an alteration in their precession frequency, and thus is also called spin-spin relaxation.

T_1 relaxation is due to an exchange of energy with the surrounding tissue, and thus is called spin-lattice relaxation. [Jung, 2013]

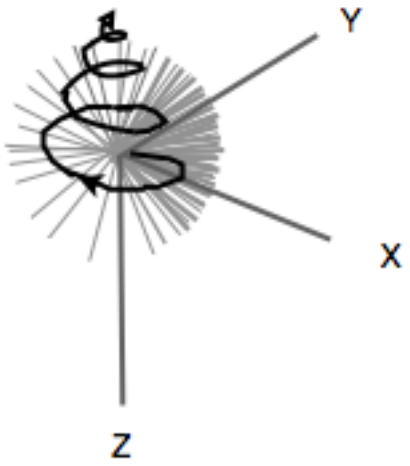

Fig 4: The net magnetic vector at time t, $M_{t,}$ undergoes relaxation, and the induced current amplitude decays with time.

2.1.8 Contrast

Image contrast results from signal intensity differences between two tissues. The property of relaxation can be exploited to produce contrast.

Although contrast agents are not visualised directly by MR, they induce inhomogeneities in the local magnetic field, and enhance relaxation of adjacent tissue spins.

This effect is due to the presence of unpaired electrons in their outer orbitals, with strong magnetic momentum, which, when placed in B_0, behave either paramagnetically or ferromagnetically, and induce local magnetic field inhomogeneities, thus affecting local proton spins. This is because the magnet moment of electrons is 657 times greater than that of protons, and requires the effect of an external magnet to overcome the spin randomisation effect of thermal motion. [Froehlich, 2006]

2.1.9 The Bloch Equation

The effect of T_1 and T_2 on nuclei in a magnetic field can be used to describe the magnetic vector. The Bloch equations are solutions of dM/dt, that can be used to explain various phenomena:

$$dM / dt = \gamma M \times B_0 - (M_x i + M_y j) / T_2 + (M_z - M_0)k / T_1$$

where $M = [M_x\ M_y\ M_z]^T$ is the magnetization, B_0 is the net magnetic field, i, j, k are unit vectors in the x,y,z directions. [Bloch, 1946; see appendix A]

2.2 Image Formation

This section deals with how the MR signal can be used to create an image.

2.2.1 ^{1}H

The hydrogen nucleus ^{1}H is prevalent in human tissue. It has one proton, and no neutrons, and thus, a net spin. [Plewes, 2012]

Magnetic resonance imaging is predominantly concerned with imaging the proton density (number of protons per volume unit) of mobile hydrogen nuclei, which have sufficiently long T2 relaxation times (i.e. greater than 10 ms) so that spatial encoding gradients can be played out between excitation and acquisition before the signal has completely decayed. [Henkelman, 2001]

2.2.2 Gradients

The homogenous main magnetic field B_0 can be altered in a linear fashion by the introduction of gradient magnetic fields.

Three gradient coils (G_x, G_y and G_z) produce linear alterations in the strength of the magnetic field experienced by tissue placed in it, in a chosen axis.

Mathematically: $B(r) = B_0 + G \cdot r$

where r is a spatial location and G is a vector of gradient field strength (in mT/m).

Thus: $\omega(r) = \gamma B(r)$

indicating that we can induce a spatial variation in the precession frequency. [Hashemi, 2010]

Fig 5: The magnetic field gradient causes spatial variation of phase.

2.2.3 Spatial Encoding

The signal acquired is the sum of the transverse magnetisation for all positions, however alteration of the precession frequency in three axis allows us to localise tissue in three dimensions.

Frequency and phase are connected in that frequency is the rate of change of phase.

We first select the z axis (slice selection), followed by y axis (phase encode) and then x axis (frequency encode).

The subsequent signals allow us to map the tissue within a slice due to its specific phase and frequency signature. [Hashemi, 2010]

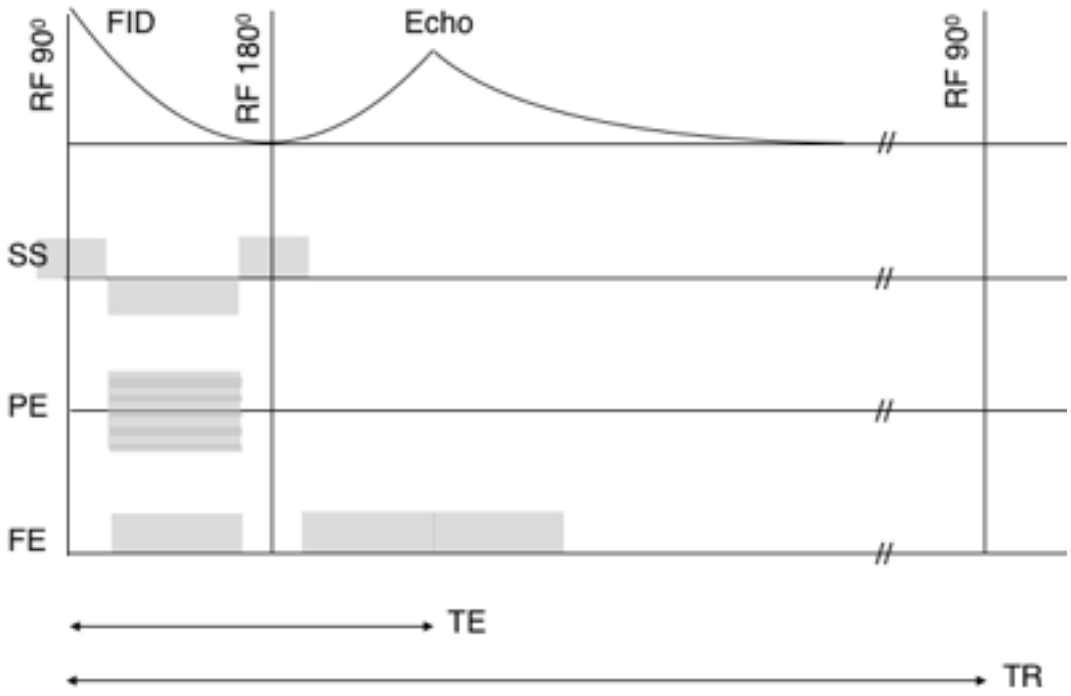

Fig 6: Spatial encoding with gradients. This is a typical spin echo sequence. The gradients are depicted in grey boxes. Note the gradient timing, and the direction of the gradients. As the gradients induce dephasing, an opposite gradient lobe must be used to ensure in-phase magnetization for maximal signal. TE = time to echo, TR = time to repetition, SS = slice select, PE = phase encode, FE = frequency encode (and readout gradient).

For each phase encode, a time (TR) passes, thus the time to acquire each slice (TS) depends on the number of phase encodes (N_{PE}) and the TR: [Ridgeway, 2010]

$$TS = N_{PE} \times TR$$

2.2.4 Fourier transform

The MR signal from the FID coil is a summation signal. It can be broken up into its constituent waveforms.

Fourier transformation is the mathematical process to separate out the individual sine and cosine waves (with different phase) into their different frequencies. [Gallagher, 2008]

Each waveform corresponds to a voxel or volume of tissue precessing at a unique phase and frequency, at a unique spatial location, induced by the gradient fields. [Bernstein, 2004]

2.2.5 K-space

Each slice of tissue is plotted in k-space. K is the wave number, and its phase and frequency components can be plotted as co-ordinates (K_x, K_y). [Paschal, 2004]

Thus each point in k-space has an associated waveform, whose amplitude is determined by the proton density of mobile hydrogen nuclei in that three dimensional volume.

The final MR image is a summation image of the weighted waveforms. This explains why each point in K-space contributes information on the entire MR image. [Westbrook, 1998]

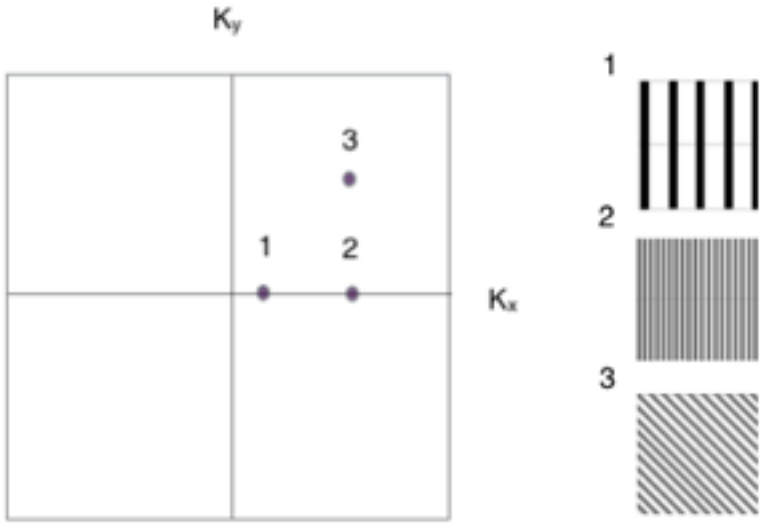

Fig 7: K-space. The plotted points in K-space and their corresponding spatial frequencies when Fourier transformed. Note that the spatial frequencies increase nearer the edge of K-space. All points are superimposed in a summated final image.

2.2.6 Reconstruction

Thus reconstruction can be summarized as the process of converting the raw data into image data.

The magnet acts as an encoding device, and the radiofrequency coils receive a superposition of all tissue signals, that, through the means of phase and frequency differences, are spatially encoded.

This superimposed data is converted from analog to a digital form as k-space data.

This k-space data can be noise pre-whitened, filtered, Fourier transformed, and coil combined. Each component has an impact on signal-to-noise (SNR) and the point spread function in the final image. [Hansen, 2014]

2.3 RF Pulse sequences

This section deals with the basic sequences of magnetic resonance.

2.3.1 Spin echo

The basic spin echo sequence of consists of a 90° pulse, applied in the x-axis, followed by one of 180°, applied in the y-axis. [Hennig, 1991]

An FID is induced by the 90° pulse. At this point T_2^* relaxation causes the decrement of the signal, induced by spin-spin and B_0 inhomogeneities.

The 180° pulse is applied at a time TE/2 after the 90° pulse, equivalent to a magnetic field in the -z axis.

The magnetic vectors which are precessing out of phase owing to B_0 inhomogeneities find the torque of these inhomogeneities reversed and thus at a time, TE (time to echo), come back into phase, inducing another current in the coil. This current is called the echo. After which the magnetic vectors dephase once again.

The spin echo sequence corrects for B_0 inhomogeneities, thus signal decay is solely due to spin-spin, T_2, relaxation. [Bitar, 2006]

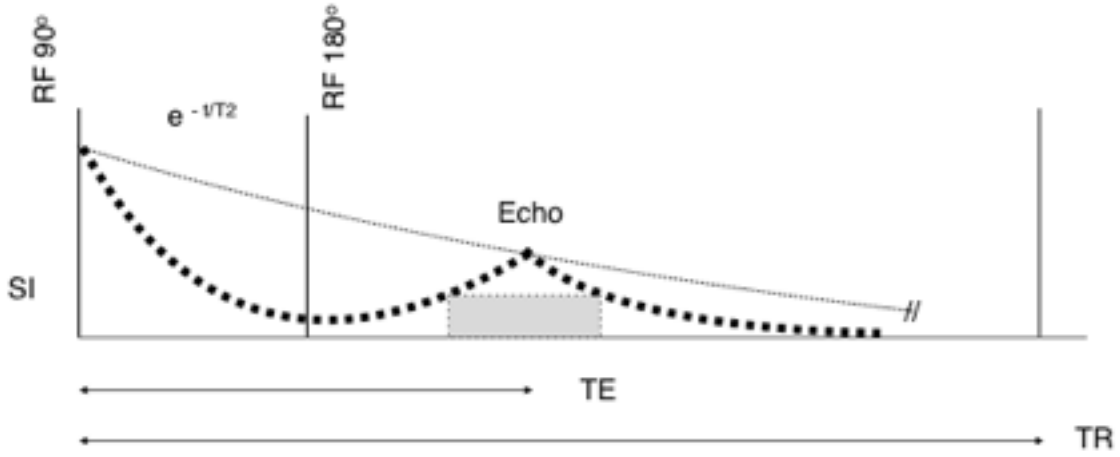

Figure 8: Spin echo formation. The FID induced by the initial 90° RF pulse decays exponentially according to $e^{-t/T2}$. The second RF pulse (RF 180°) occurs at TE/2. SI = signal intensity, TE = time to echo, TR = time to repetition. Readout gradient in grey box.

2.3.2 Turbo spin echo

To image faster, the signal can be refocused many times with 180° pulses, with each echo having a different phase encoding gradient.

This is called an echo train, and the number of echoes per TR is the echo train length, or turbo factor (TF), which is the denominator by which the acquisition time for the slice is shortened:

$$TS = (N_{PE} \times TR) / TF$$

where TS = time to acquire each slice, N_{PE} = the number of phase encodes

This type of sequence is also called rapid acquisition with relaxation enhancement (RARE), or fast spin echo (FSE), or turbo spin echo (TSE). [Tsao, 2010]

2.3.3 Gradient Echo

The key concept of gradient echo is the use of polar gradients, rather than 180° pulses, to refocus the magnetic vectors. The frequency, or readout gradient, is used to dephase and rephase the MR signal, and thus create an echo. [Hennig, 1991]

Thus one RF pulse, rather than two in the case of the spin echo technique, is used, which is quicker but less efficient, as the refocusing cannot correct for local B_0 inhomogeneities, leading to more rapid dephasing and loss of signal.

Neither technique correct for the dephasing effects of local spin-spin interactions (T_2).

The decay time seen in gradient echo (T_2^*) is described by the relationship:

$$1/T_{2^*} = 1/T_2 + 1/T_{2'}$$

where $T_{2'}$ is the dephasing effect of local B_0 inhomogeneities. [Hahn, 1950]

The sequence uses a pulse that gives a variable flip angle (up to 90°). After this a negative gradient field is applied, causing dephasing. This is followed by a positive gradient field, or lobe, causing rephasing and generates an echo. [Markl, 2012]

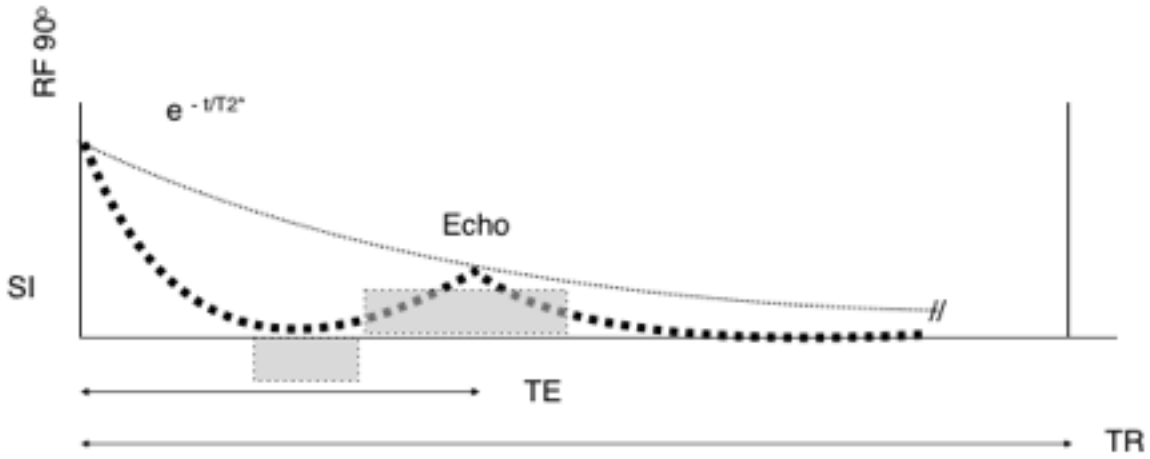

Figure 9: Gradient echo formation. The FID induced by the initial 90° RF pulse decays exponentially according to $e^{-t/T2^*}$. The signal is dephased and rephased (recalled) with bipolar gradients (in grey boxes). The second gradient is the readout gradient. SI = signal intensity, TE = time to echo, TR = time to repetition.

2.3.4 Steady state free precession

In order to image faster, the TR may be shortened. If this occurs before complete longitudinal magnetization recovery, a condition called the steady state may occur, in which the magnetization available is the same from one TR to the next. [Carr, 1958]

The magnetization available in the steady state (Mss) can be calculated by the Ernst formula:

$$Mss = M0\ (1 - e^{-TR/T1} / 1 - e^{-TR/T1} \cos \alpha)$$

where TR is the RF pulse repetition time, and α is the flip angle. [Ernst, 1987]

When TR is shortened to the point of $TR < T_2$ there will be residual transverse magnetization before the next RF pulse. This may be resolved by spoiling,

[Scheffler, 2003] or balancing the gradients (the net gradient induced dephasings is zero). [Oppelt, 1986]

2.3.5 Inversion Recovery

Inversion Recovery is a sequence used to null the signal from a particular tissue.

It consists of a 180° pulse, which is followed by a 90° pulse after a time of inversion (TI), and hence by a 180° refocusing pulse, similar to a spin echo sequence. [Bitar, 2006]

The magnetic vectors will relax back to B0 at a rate determined by their T_1.

For example, the T_1 of fat is shorter than that of water. Thus if the TI of fat is chosen, then the 90° pulse will flip its net vector back to 180° where it will not contribute to the signal.

The T_1 of water is longer and thus the 90° pulse will produce a signal.

Thus tissues can be distinguished according to their T_1, or TI. This is called weighting.

Any soft tissue can be suppressed by choosing TI to be 0.693 times the T_1 of that tissue ($\log(2) \times T_1$). [Redpath, 1994]

If a short TI is chosen, one can null the signal from fat; this is called STIR, or short tau inversion recovery.

If a longer TI is chosen, once can null the signal from water; this is called FLAIR, or fluid attenuated inversion recovery. [Westbrook, 2003; de Coene,1992]

2.3.6 Double Inversion Recovery

A second inversion pulse allows two tissues to be nulled simultaneously; this is called a double inversion recovery (DIR) sequence. [Bydder, 1985]

This requires knowledge of the T_1 of the tissues to be nulled, and a difference in their respective relaxation times.

In the heart, this is known as black blood imaging, as the first inversion pulse inverts all the spins in the body (non-selective), and a second (slice selective) pulse immediately re-inverts the spins in the slice of interest. Blood spins outside the slice of interest are still inverted but slowly relax according to their T_1. When the spins of the blood in the slice of interest are nulled (at TI), the selected image sequence proceeds, affording maximum contrast between blood and adjacent structures. [Edelman, 1991; Simonetti, 1996]

Thus double inversion is a preparatory sequence that maximises tissue contrast, and is used in the studies that follow in this thesis.

Triple and quadruple contrast have been described. [Yarnykh, 2002; O h-Ici, 2012]

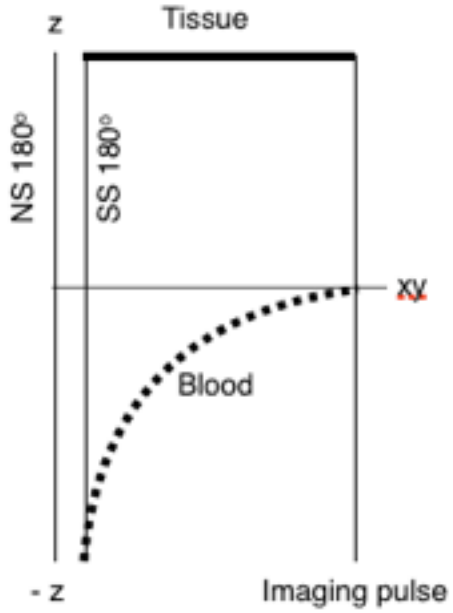

Figure 10: The evolution of transverse magnetisation (bold lines) during a black blood DIR preparatory sequence. NS = non-selective, SS = slice selective pulses.

3 Thoracic imaging With MRI

3.1 Thoracic MRI

This section deals with the benefits and drawbacks of MR imaging of the thorax.

3.1.1 Comparison with CT

Compared to CT, MR shows superiority in five main areas. It shows superior soft tissue contrast; superior temporal resolution; it lacks ionizing radiation; it does not require ionic media to produce contrast; and it also has potential to combine morphological with functional imaging.

3.1.2 Motion artifact

MRI of the thorax is affected by motion artifacts, due to respiration and cardiac activity, and limited by its temporal resolution.

3.1.3 Signal-to-noise ratio

Thermal noise affects MR measurements, having a mean value of zero and a standard deviation. The raw data is comprised of two components, signal and noise. The signal intensity of a pixel is affected by the standard deviation of the noise at the spatial location.

Its impact is referred to as the signal-to-noise ratio (SNR), defined as:

$SNR(x, y) = SI(x, y) / N(x, y)$

where S(x, y) is the signal intensity at pixel location (x, y) and N(x, y) is the standard deviation of the noise at that pixel location. [Hansen,2014]

The lung is predominantly composed of air, yielding a low density of protons, and thus a weaker signal, or SNR, compared with other anatomical structures. [Biederer, 2010]

Thus, lungs will usually appear without any visible signal on conventional MR images.

3.1.4 Tissue interfaces

The lung has many air-tissue interfaces leading to local magnetic field inhomogeneities, and thus rapid T2* dephasing of the low signal. [Su, 1995]

3.1.5 Potential solutions

Respiratory motion artifact can be overcome by the use of breath-holding (apnea), or respiratory gating, typically by the use of a pneumatic belt.

Cardiac motion, which is not under voluntary control, can be surmounted by faster imaging techniques such as fast spin-echo imaging using half-Fourier acquisition (e.g. T2-HASTE) or very short echo times (e.g. ultra fast turbo-spin-echo, UTSE).

[Leutner, 1999] Alternatively, lung images can be acquired using ECG-gated image acquisitions, effectively eliminating cardiac pulsation artifacts. I utilized this approach in the studies of this thesis.

Spin dephasing at tissue interfaces leads to very short T2* times, averaging about 1.5 ms, depending on lung volume. [Theilmann, 2009], necessitating repetition times (Tr) shorter than T2* when imaging with gradient echo. However assuming constant lung volume, given that the magnetic inhomogeneities are static, the signal can be rephased with fast spin echo techniques, leaving a T2 that is much longer than T2* in the lung, and similar to that of other tissues. [Millera, 2014]

Proton density and thus lung signal intensity are increased with lung deflation, thus imaging at end-expiration is helpful. [Biederer, 2010]

Parallel imaging can lead to further diminution of examination times and thus potential reduction in motion artifact [Heidemann, 2003], as can new sequence designs such as periodically rotated overlapping parallel lines with enhanced reconstruction (PROPELLER), that provide inherent motion insensitivity. [Pipe, 1999]

3.1.6 Parallel imaging

Acceleration with parallel imaging is used in the studies in this thesis to reduce scan times and motion artifact.

Scan time (T) is a product of the number of phase encoding steps (y-axis) and the repetition time (time taken for the frequency encoding step, x-axis).

An additional multiplier is accrued if the sequence is performed in 3D, as a partition encoding step is added (z-axis). [Deshmane, 2012]

Parallel imaging is a reconstruction technique that uses partial sampling, reducing the number of phase encoding steps, thus reducing scan time.

Parallel imaging uses additional spatial information from phased-array coils, in addition to phase and frequency, to fill in the partially sampled k-space (GRAPPA, generalized auto-calibrating partially parallel acquisition), [Griswold, 2002] or to create an unaliased final image out of the aliased image imposed by the partial sampling technique (SENSE, sensitivity encoded). [Pruessmann, 1999]

The maximum theoretical time reduction factor (R) equals the number of elements in the phased-array coil. [Noel, 2009]

The use of massively parallel imaging is being investigated, using up to 64-channel array coils. [Keil, 2013]

Parallel imaging has been used to investigate function [Emami, 2013], and structure of the lung. [Gorkem, 2013]

3.1.7 Half-Fourier acquisition

K-space exhibits symmetry. Each co-ordinate in k-space has a mirror image across its origin, as opposite locations are complexly conjugated.

The signal intensity of a point on one side of an echo obtained using a positive phase-encode step is the complex conjugate of that on the other side of an echo obtained using the corresponding negative phase-encode step. [Feinberg, 1986]

This property implies that reconstruction of an image can be performed by acquiring only half of the rows of k-space data.

Half-Fourier-acquisition single-shot turbo spin-echo (HASTE) is used to image the lung, significantly reducing acquisition times. [Fink, 2007; Henzler 2009]

3.1.8 Generic pulmonary imaging protocols

Recommended protocols have been published [Biederer, 2010; Puderbach, 2010] and are based on parallel acquisition techniques, but multi-breath hold acquisitions can be used instead.

A typical protocol begins with a gradient recalled echo (GRE) localizer in inspiration to plan the study.

The first sequences are acquired in breath-hold, usually starting with the coronal T2-HASTE (half-Fourier acquisition single-shot turbo spin-echo) [Hatuba, 1996], which will provide good signal of inflammatory disease [Puderbach, 2007] despite partial Fourier acquisition and long echo trains.

This is followed by a transverse T1-3D-GRE (VIBE, volumetric interpolated breath examination) to image solid lung lesions, nodules and the mediastinum. [Biederer, 2010; Hekimoglu, 2010]

Next a coronal T1/T2-weighted, free breathing SS-GRE sequence (steady state GRE eg. TrueFISP) is acquired, allowing recovery from the breath-hold maneuvers. Pulmonary and cardiac motion information can be generated. Healthy lung parenchymal signal on SS-GRE is higher than on the first two sequences of the protocol. [Biederer, 2010]

A short tau inversion recovery (STIR) sequence can be acquired using a multiple breath-hold technique, and aides the detection of mediastinal lymph nodes.

The final acquisition is a single slice dynamic SS-GRE series for diaphragmatic function, focusing on the highest elevation of the diaphragmatic dome to be acquired

with an ideal temporal resolution of 3–10 images per second. The patient is asked to breathe deeply.

This basic protocol takes about 15 min. Specific variations of the protocol and additional series can be added as indicated.

Contrast can be used to improve the diagnostic yield of 3D-GRE sequences by clearer depiction of vessels, hilar structures and pleural enhancement.

Contrast-enhanced perfusion MRI using T1-weighted ultra-short TR and TE gradient echo MRI [Hatabu, 1996] can be used in combination with SS-GRE sequences to evaluate for pulmonary emboli. [Kluge, 2006]

Ventilation can be investigated using imaging using oxygen enhancement [Ohno, 2001], or hyperpolarised noble gases. [Fain, 2010]

3.1.9 Paramagnetic contrast agents

The contrast medium used most frequently is a chelate of gadolinium. It is a paramagnetic, trivalent, lanthanide element with seven unpaired electrons, with a large magnetic moment, and ability to influence the relaxation times of adjacent water molecules. It has a low molecular weight allowing it both intravascular and extracellular space distribution. [Sherry, 2009]

Adequate timing of the contrast agent administered by an automatic power injector is essential to achieve high contrast between pulmonary artery branches and surrounding structures, thus ensuring optimal gadolinium (Gd) concentration at the time of central K-space acquisition, and best signal.

3.2 Pulmonary Applications of MRI

This section deals with the use of MRI in specific disease entities, particularly the potential to influence decision-making in pulmonary medicine.

3.2.1 Lung nodules

MRI is more accurate than CXR in detecting nodules > 5 mm. [Vogt, 2004] Its sensitivity for nodules < 5 mm is low, but almost 100% for nodules ≥ 8 mm. [Bruegel, 2007; Biederer, 2008] It is less sensitive than MDCT for nodule detection, the current gold standard.

T1 and T2 weighted MRI do not reliably discriminate between benign and malignant nodules. [Fan, 2014] Other MR sequences are needed to take advantage of malignant biology.

Malignant nodules demonstrate restricted diffusion. A meta-analysis of 10 studies that looked at the diagnostic accuracy of diffusion weighted imaging (DWI) to distinguish between benign and malignant pulmonary nodules showed a pooled positive likelihood ratio of 5.3 (95% CI, 2.1–13.0) and a negative likelihood ratio of 0.19 (95% CI, 0.12–0.30). [Wu, 2013]

Malignant nodules demonstrate angiogenesis. Dynamic contrast enhanced MRI (DCE-MRI) demonstrates differences in microvascular hemodynamics between benign and malignant nodules. Various protocols have been used looking at signal intensity changes.

Ohno, using relative contrast enhancement ratios, has shown 100% accuracy in differentiating solitary pulmonary nodules (SPNs) into those that do and do not

nescessitate further evaluation. [Ohno, 2002]; although a recent study did not confirm this. [Satoh, 2013]

However a meta-analysis of 44 trials demonstrated that DCE-MRI, DCE-CT, positron emission tomography (PET), and single-photon emission computed tomography (SPECT) have similar diagnostic accuracy. [Cronin 2008]

Currently DCE-MRI is the MR modality of choice to help differentiate between benign and malignant pulmonary nodules.

3.2.2 Lung cancer

The goal of lung cancer imaging is to provide accurate information on local (T stage), lymphatic (N stage), and distant spread (M stage). PET/CT is currently the clinical standard in the staging of lung cancer.

MR images have poorer spatial resolution than CT images. Thus MRI has shown itself to be as sensitive as CT in differentiating between T3 and T4 tumors, [Wielputz, 2012] but inferior in the detection of small satellite nodules in the same pulmonary lobe (T3) or alternate ipsilateral lobe (T4). [Yoon, 2014]

However as MRI allows tissue characterisation and the ability to determine the integrity of fat planes, MRI is more accurate in identifying mediastinal and hilar invasion. [Ohno, 2004]

MRI is the imaging method of choice to evaluate and determine the resectability of non-small cell lung cancer (NSCLCa) of the superior sulcus (Pancoast tumor). [Bilksy, 2002]

N-staging is the most important prognostic factor in determining survival. Invasive mediastinoscopy is considered the gold standard. Non-invasive imaging uses a short-axis size cut-off of 10 mm to determine nodal involvement, however this is

neither sensitive, as normal-sized nodes may be involved, nor specific, as nodal enlargement occurs secondary to inflammatory processes. [Fan, 2014]

Malignant biological characteristics may be visualized with MR techniques. DWI has shown similar or improved accuracy in correct N staging of lung cancer when compared to PET/CT, the current reference standard for non-invasive nodal staging. [Yi, 2008; Wu, 2012]

Glucose utilisation in the brain reduces the specificity of PET imaging for M-staging. PET will miss 39% of the cerebral metastases that MRI will identify. [Rohren, 2003]

Yi showed that 3.0T whole-body MR imaging (WB-MRI) was comparable to PET/CT in M-staging, and more useful for detecting brain and hepatic metastases, whereas PET/CT is more useful for detecting lymph node and soft-tissue metastases. [Yi, 2008]

Thus a multi-modal imaging approach may be the current optimum staging protocol.

3.2.3 Pulmonary embolism

A comparative study, of three MR techniques (SSFP, contrast-enhanced MR angiography, and MR perfusion imaging) yielded high the sensitivity and specificity for pulmonary embolism (PE), comparable to multi-dectector computed tomography (MDCT). [Kluge, 2006]

However a large multi-center study comparing MR angiography and venography with MDCT demonstrated limited sensitivity owing to inadequate imaging technique. [Stein, 2010]

MRI has not supplanted CT as the imaging modality of choice for PE. It is an alternative in those cases where radiation or iodinated contrast agents are not preferred.

3.2.4 Airway diseases

MR techniques have used hyperpolarised (or magnetised) noble gases (^{3}He, ^{129}Xe) [Dregely, 2011; Fain, 2010] as a means of imaging ventilation. It allows regional dysfunction to be visualised, not apparent on averaged pulmonary function testing values. [Bannier, 2010]

The use of apparent diffusion coefficients (ADC) with ^{3}He may identify early changes in lung microarchitecture, and those at-risk asymptomatic smokers. [Fain, 2006]

More recently, inert fluorinated gas (^{19}F) has been investigated as an alternative to hyperpolarised gas, to measure regional ventilation, gas exchange and lung microstructure, as it is cheaper and offers similar performance. [Couch, 2014]

Techniques with high temporal resolution (time resolved FLASH or trueFISP) have been used to demonstrate lung mechanics. [Tokuda, 2009]

There is growing evidence that MRI demonstrates high concordance with MDCT to detect the lung morphological changes in patients with CF. [Puderbach, 2007; Puderbach 2007; Sileo 2014]

3.2.5 Interstitial lung disease

McFadden et al, in 1987, were the first to show a potential role for MR in interstitial lung disease, using a 0.15 T magnet. [McFadden, 1987]

In 1992, Muller et al showed inferiority compared to HRCT in anatomical depiction of fibrosis, but comparable in demonstrating air space opacities, using a 1.5T magnet. [Muller, 1992]

Several studies focused on tissue characterisation, with the aim of distinguishing active alveolitis from inactive fibrosis.

Most of these studies focused on the enhancement pattern seen with the administration of macromolecular contrast agents. Lesions with active alveolitis showed prominent enhancement, whereas fibrotic lesions did not. [Berthezene 1992; Gaeta, 2000]

This was confirmed in high-field/3T MR, demonstrating an early enhancement pattern in inflammation-predominant lesions on dynamic MRI. This is presumably due to an increased extravascular interstitial space with abundant inflammatory cell infiltrates or promotion of neo-vascularization with increased angiogenesis in those lesions. [Yi, 2008]

A retrospective study of 46 patients with pulmonary fibrosis using a 1.5 T scanner compared CT images with two-dimensional balanced steady-state free precession (bSSFP) acquisitions and showed a sensitivity and specificity of 89% (95% confidence interval: 77%, 96%) and 91% (95% confidence interval: 76%, 98%), respectively. [Rajaram, 2012]

4 The imaging of sarcoidosis

4.1 Biological

This section deals with the biological and clinical features of sarcoidosis

4.1.1 Etiology

Sarcoidosis is a granulomatous disease of unknown etiology.

The immunopathogenesis of sarcoidosis is not completely understood. The pathogenesis of sarcoidosis seems to involve exposure to one or more exogenous antigens, as well as predispository HLA class II molecules, and T-cell receptors leading to a cellular recruitment, proliferation, and differentiation and the formation of the sarcoid granuloma. [Iannuzzi, 2007]

4.1.2 Histology

The granuloma is characterised by a core of monocyte-derived epithelioid histiocytes and multinucleate giant cells with interspersed CD4 T lymphocytes, which have a Th1 lymphocyte phenotype.

4.1.3 Diagnosis

The diagnosis of sarcoidosis is arbitrarily made when the statistical likelihood of alternative diagnoses becomes too small to warrant further investigation. Therefore, sarcoidosis is a diagnosis of exclusion. [Baughman, 2011]

The diagnosis is established when clinico-radiographic findings are supported by histologic evidence of non-caseating granulomatous inflammation and other causes of granulomas and local reactions have been reasonably excluded. [Hunninghake, 1999]

Endobronchial ultrasound (EBUS) has significantly improved the diagnostic yield compared to transbronchial needle aspiration (TBNA). [Tremblay, 2009]

4.1.4 Clinical features

The lungs are affected in more than 90% of patients with sarcoidosis. Approximately 20% develop chronic lung disease leading to pulmonary fibrosis. Pulmonary function testing is non-diagnostic although restrictive physiology is usually observed. Airway obstruction may be seen, as well as a reduction of diffusing capacity.

4.1.5 Treatment

Treatment of sarcoidosis is usually limited to the symptomatic patient, but the decision to treat is limited by the ability to predict who will need long-term therapy.

Corticosteroids are still the first line of treatment, a paradigm that has been stable since cortisone was first used in 1951. [Siltzbach 1952; Sones, 1951]

The response to corticosteroids will determine the need for immunosupression, and patient characteristics and clinical phenotype will influence the choice of agent used.

Current treatment practices are based on small randomized controlled trials, case reports, or analyses of case series. Studies of therapy have shown short-term disease modulation [Paramothayan 2005, 2003] but inconsistent long-term benefit. [du Bois, 1994]

Of the alternative agents, methotrexate is considered the preferred second-line agent, [Judson, 2012] with similar activity to steroids in acute disease. [Baughman, 1990]

Biological agents have shown some success [Baughman, 2009].

Sarcoidosis-associated pulmonary hypertension may respond to vasomodulatory agents. [Baughman, 2011]

4.2 Radiology of sarcoidosis

This section deals with the imaging of sarcoidosis

4.2.1 Chest radiography

The chest roentgenogram (CXR) is the initial test, given that sarcoidosis affects the thorax in 90% at some time in the disease process. [Nunes, 2007], although those with histologically proven pulmonary sarcoidosis may have a normal CXR. [Ortega, 2011]

CXR was used to radiographically stage pulmonary sarcoidosis in 1961 [Scadding, 1961], and has since been modified.

The classification schema defines the following stages: stage 0: no adenopathy or infiltrates; stage 1: hilar and mediastinal adenopathy alone; stage 2: adenopathy and pulmonary infiltrates; stage 3: pulmonary infiltrates alone; and stage 4: pulmonary fibrosis.

This staging system is plagued by interobserver variability [Baughman, 2011] and is insensitive to clinical changes. [Judson, 2008] It has some prognostic implication [Hunninghake, 1999] though it may be inaccurate in suggesting a biological sequence.

4.2.2 Computed tomography

CT is superior chest radiographs in depicting parenchymal, mediastinal, and hilar structures. [Koyama, 2004].

Collimation widths of 0.6 mm provide optimal spatial resolution. Image reconstruction with a high-spatial-frequency algorithm improve parenchymal definition. Administration of contrast agents is useful to depict lymphadenopathy. [Nunes, 2007]

Radio-pathological correlation has established that the characteristic thickened bronchovascular bundles and small perivascular nodules, characteristically in the upper and middle zones, seen at CT correspond to granulomatous infiltration within the peribronchovascular connective tissue sheath. [Ortega, 2011]

Honeycomb-like cysts, bullae, broad and coarse septal bands, architectural distortion, volume loss, and traction bronchiectasis are indicative of irreversible fibrosis. [Criado, 2010]

Ground-glass opacities represent granulomatous accumulation, rather than alveolitis, below the spatial resolution of CT to detect individually. [Nishimura, 1993] This can be stated once superimposed infection has been excluded.

CT scanning has not shown the ability to cross-sectionally reliably discriminate active inflammation from fibrosis. [Remy-Jardin 1994; Leung, 1998]

4.2.3 Gallium scanning

The sensitivity of ^{67}Ga scan in pulmonary sarcoidosis is 60 to 90%. The ‘lambda’ and ‘panda’ appearances of ^{67}Ga uptake in sarcoidosis are characteristic, however isolated patterns lack specificity. [Nunes, 2007]

4.2.4 Positron emission tomography

^{18}FDG is used to detect high glucose metabolism and has been shown to be useful for the assessment of inflammatory activity in sarcoidosis. [Keijsers, 2011]

PET can be useful in monitoring therapeutic response, as FDG is taken up by active sarcoidosis [Prabhakar, 2008]

4.2.5 Magnetic resonance imaging

This section deals with MR imaging of the heart and lungs in sarcoidosis

4.2.5.1 MRI of cardiac sarcoidosis

CMR is well established and preferred over positron emission tomography (PET) in the evaluation of cardiac sarcoidosis owing in part to a higher specificity, and lack of radiation. [Ohira, 2008]

CMR uses a T2 weighted signal and early gadolinium images to detect acute inflammation and late gadolinium enhancement with T1 weighting to assess for fibrosis or scar. The findings vary depending on the stage of the pathological process. [Zipse, 2014]

Surveillance with CMR may be used to assess the efficacy of steroid therapy [Vignaux, 2002].

In a cohort of 61 patients who met the histological and clinical criteria for sarcoidosis without cardiac disease, 13% showed evidence of late gadolinium enhancement using routine contrast enhanced cardiac sequences. [Nagai, 2014]

The most common manifestations of cardiac sarcoidosis include atrioventricular conduction defects and branch blocks, followed by sustained and non-sustained ventricular tachycardia and atrial arrhythmia. [Habersberger, 2008]

No studies have assessed a sequence to establish the coexistence of cardiac and thoracic sarcoidosis.

4.2.5.2 MRI of thoracic sarcoidosis

Several authors have studied thoracic MRI in sarcoidosis, focusing on unenhanced T1 and T2 weighting. [Muller, 1992; Craig, 1988; Primack, 1994; McFadden, 1987; Mendelson, 1992]

Gaeta was the first one to use contrast enhancement, in a cohort of patients with ILD, 10 of which had sarcoidosis, and demonstrated early enhancement of active pulmonary lesions. [Gaeta, 2000]

In 2007 Luttebey demonstrated that a T2 turbo spin echo (TSE) sequence in a 3T scanner out-performed CT in demonstrating disease activity. 8 of 21 patients had sarcoidosis. [Luttebey, 2007]

In 2013 Chung was the first to systematically compare CT to MRI in pulmonary sarcoidosis, using a multi sequence approach (VIBE, HASTE, TrueFISP, BLADE). The post contrast VIBE images were taken 60-90 sec after bolus. They concluded that MRI and CT showed good agreement. There was weaker correlation for small nodules, fine reticulation, similar to the findings by Rajaram, owing to inherent lower spatial resolution of MRI. There was also poorer agreement in the lower lobes, perhaps explained by motion artifact. This was a retrospective study and they allowed 90 days between image studies. [Chung, 2013; Rajaram, 2012]

There is no data concerning late enhancement pertaining to pulmonary lesions in sarcoidosis; though it has been used to evaluate cardiac lesions of sarcoidosis. [Tadamura, 2005]

5 The imaging of idiopathic pulmonary fibrosis

5.1 Biological

This section deals with the biological and clinical features of IPF.

5.1.1 Etiology

IPF belongs to a family of lung disorders known as the interstitial lung diseases (ILD) /diffuse parenchymal lung diseases (DPLD).

Within this broad category of diffuse lung diseases, IPF belongs to the subgroup known as idiopathic interstitial pneumonia (IIP). There are seven distinct IIPs, differentiated by specific clinical features and pathological patterns. IPF is the most common form of IIP.

The immunopathogenesis are incompletely understood. It can be conceived as a primarily fibrotic process, as evidenced by inflammatory paucity on histology and lack of steroidal response. Environmental and genetic factors may contribute to a vulnerable alveolar epithelium, leading to fibrogenesis. [Noble, 2012; Günther, 2012]

Cigarette smoking is strongly associated with IPF. One study reported a correlation between smoking history (20–40 pack-years) and risk for IPF, with an odds ratio of 2.3 (95% confidence interval, 1.3 to 3.8) for smokers. [Meltzer, 2008]

5.1.2 Histology

UIP is defined by the presence of microscopic honeycombing, fibroblastic foci, and a variegated pattern of chronic interstitial fibrosis with accentuation beneath the pleura.

The origin of pathological fibroblast foci within the IPF is unclear. Possibilities include differentiation of resident fibroblasts, recruitment of circulating fibroblast precursors and transdifferentiation of epithelial cells into pathological fibroblast phenotypes. [Meltzer, 2008]

5.1.3 Diagnosis

The diagnostic criteria for IPF require exclusion of known causes of interstitial lung disease (associated connective tissue disease, drug toxicity or environmental exposure). [ATS/ERS Consensus statement, 2010]

The diagnosis can be established by typical clinico-radiographic findings, in the absence of histopathological confirmation. [Meltzer, 2008; Raghu, 2011]

5.1.4 Clinical features

Progressive lung fibrosis impacts the alveolar gas exchange leading to reduced diffusing capacity, and ventilation perfusion mismatch. Exertional dysponea is typically progressive, and patients may manifest digital clubbing, and a bothersome dry cough.

Gastro-esophageal acid reflux is present in close to 90% of patients with IPF but often occurs without symptoms.

As scar tissue accumulates, lung compliance is reduced and restrictive physiology becomes manifest on lung function testing.

Evidence of right heart failure as a result of pulmonary hypertension may develop. [Meltzer, 2008]

5.1.5 Treatment

When UIP patterns are demonstrated on chest CT scan and lung biopsy, treatment with immunosuppressive therapy such as prednisone and azathioprine is ineffective. [Noble, 2012]

There is evidence to show that pirfenidone (which mitigates fibroblast proliferation, fibrosis-associated proteins and cytokines, and the biosynthesis and accumulation of extracellular matrix, as well as accumulation of inflammatory cells and TNF-a synthesis) improves decline in function. [Cottin, 2012]

A recent trial of perfenidone, in those with mild-to-moderate disease, confirmed a reduction in decline of function over placebo. [King, 2014]

Biological therapy that acts on different receptors have shown promise. A recent phase-2 trial of a tyrosine kinase inhibitor (nintedanib) demonstrated a reduction in decline of lung function. [Richeldi, 2014]

Inclusion in a randomised controlled trial or assessment for transplantation is usually appropriate, the later providing survival benefit for select patients. [Kistler, 2014]

The overall prognosis is poor in IPF, and rate of progression remains difficult to predict, though several biomarkers, whose levels do not correlate with disease severity, show promise. [Ley, 2011]

5.2 Radiology of IPF

This section deals with the imaging of IPF

5.2.1 Chest radiography

The chest radiograph is abnormal in most patients with IPF, demonstrating bilateral asymmetrical reticular markings with a basal propensity, interspersed between areas of focal round translucency representing honeycombing. However, diagnosis is limited by poor interobserver agreement and diagnostic accuracy.

Approximately ten percent of patients with histologically proven IPF have a normal roentograph. [Ley, 2011]

5.2.2 Computed Tomography

High-resolution CT (HRCT) allows for radiographic characterisation of suspected interstitial lung disease.

The latest diagnostic guidelines for IPF include the presence of a usual interstitial pneumonia (UIP) pattern on HRCT scans in individuals not subjected to surgical lung biopsy. [Raghu, 2011]

The features of a classical UIP pattern on HRCT require: 1) the presence of subpleural abnormalities, predominantly basal; 2) reticular abnormality; 3) honeycombing with or without traction bronchiectasis; and 4) the absence of

features that are inconsistent with a UIP pattern (upper or middle lobe predominance, peribronchovascular predominance,
extensive ground-glass abnormality (greater than reticular abnormality), profuse micronodules, discrete multiple cysts away from areas of honeycombing, diffuse mosaic attenuation/air trapping, or consolidation in bronchopulmonary segment(s)/ lobe(s). [du Bois, 2012]

HRCT is more sensitive than measurements of pulmonary function and cardiopulmonary exercise test parameters in identifying subjects with asymptomatic ILD. [Ley, 2011]

However, significant interobserver variation exists in identification of honeycombing. [Watadani, 2013]

In one study, emphysematous change lead to the incorrect diagnosis between UIP and nonspecific interstitial pneumonia (NSIP) in more than half of the cases [Akira, 2009].

5.2.3 Magnetic resonance imaging of IPF

McFadden initially studied a group of patients with interstitial lung disease (ILD), 19 of which had IPF, with a 0.15 T magnet, using unenhanced T1 and T2 weighting, but failed to differentiate active from inactive disease. [McFadden, 1987]

Several authors subsequently studied disease activity in ILD, focusing on unenhanced sequences. In 5 patients with IPF, parenchymal opacification correlated to pathological activity (lung biopsy). [Primack, 1994] In 6 patients with IPF, proton density-weighted and T1-weighted images were comparable to CT scans in the assessment of air-space opacification. [Muller, 1992]

Gaeta was the first one to use contrast enhancement, in a cohort of patients with ILD, 4 of which had usual interstitial pneumonia (UIP), and demonstrated early enhancement of active pulmonary lesions. [Gaeta, 2000]

Lutterbey evaluated 3T MRI compared to CT in 21 patients with ILD, 1 of which had IPF. He used an unenhanced T2 weighted fast spin echo sequence, and classified activity based on signal intensities. MR outperformed CT (75% v 58%) in the determination of activity.

A limitation of this technique is false positives as a result of slow flowing blood in the pulmonary vessels, despite cardiac triggering, mimicking small inflammatory foci. [Lutterbey, 2007]

Yi used dynamic 3 T MRI in 10 patients with UIP who underwent surgical biopsy, using a T2-weighted triple-inversion black blood turbo spin-echo (TSE) sequence, compared to contrast enhanced T1 images, and showed early enhancement to be useful to differentiate inflammation predominant and fibrosis predominant pulmonary lesions.

Only 41% of the fibrosis-predominant lesions exhibited enhancement in the delayed phase. [Yi, 2008]

There is no other data concerning late enhancement in IPF.

6 Tissue characterisation of lung fibrosis

6.1 Pulmonary fibrosis

The next section deals with tissue characterisation of lung fibrosis using late enhancement techniques.

6.1.1 Fibrosis

Fibrosis is the development of excess fibrous extracellular matrix, predominantly type I collagen, in a tissue as a result of a reparative or reactive process. Extracellular fibrosis can be enhanced using gadolinium-based multimers. Collagen-specific contrast agent can also be used to visualise fibrosis. [Caravan, 2007]

6.1.2 The basis of late enhancement

Contrast enhancement using gadolinium chelates is based on T1-shortening and the distribution of contrast agent within the tissue. The mechanism of enhancement relates to the different wash-in and wash-out kinetics of normal and abnormal tissue.

A bolus of an extracellular gadolinium contrast agent (large molecular weight) will reach tissue compartments at different rates until a dynamic steady state is reached.

The differences in fractional distribution volume for ischemically injured and normal myocardium has been determined, using repetitive echo-planar imaging in experimental animals, to be 0.2 in normal myocardium and greater than 0.9 in infarcted myocardium. [Wendland, 1998]

In the case of acute myocardial infarction (MI) with rupture of the cell membrane, the gadolinium enters the extracellular space and what had previously been intracellular space. For chronic MI with cell replacement by a matrix of collagen the extracellular space is substantially increased.

There is a linear relationship between the relaxation rate of longitudinal magnetization and the change in contrast agent concentration. [Ordovas, 2011]

6.1.3 Imaging of late enhancement

The key to imaging is to achieve optimal contrast between tissues of different character.

In cardiac MR (CMR) inversion recovery (IR) preparatory sequences are used to distinguish tissues with varying T1.

A comparison of T1-weighted late enhancement sequences from the standpoint of contrast-to-noise ratio (CNR) and contrast-enhancement ratio (CER) demonstrated that IR sequences provided the best CNR and CER, when compared with other T1-weighted methods [Simonetti, 2001]

The inversion recovery time (TI) is typically chosen to null the normal myocardium, which provides the best tissue contrast between MI and normal myocardium in the case of magnitude image reconstruction. Normal myocardium will appear dark, and

the MI with higher gadolinium concentration and consequently shorter T1 and faster recovery will yield a high signal. [Kellman, 2012]

The TI may be determined by multiple acquisitions on a trial and error basis or by means of a cine-IR-SSFP scout.

A new method that is relatively insensitive to TI is phase-sensitive inversion recovery (PSIR), that uses phase information, which is discarded in the magnitude image reconstruction (giving a modulus signal intensity), preserving polarity, and increasing the contrast between tissues of varying T1. [Huber, 2005]

6.2 Tissue characterisation of lung fibrosis

The next section deals with tissue characterisation of lung fibrosis in sarcoidosis and IPF, the two fibrotic cohorts imaged in the studies which follow, and the rationale for the studies.

6.2.1 Characterisation of lung fibrosis in sarcoidosis

Accurate imaging detection and quantification of fibrotic pulmonary sarcoid is important for diagnosis, treatment and prognosis. [Hunninghake, 1999; Baughman, 2011; Spagnolo, 2014]

The gold-standard non-invasive imaging test remains chest CT, which is now widely utilised worldwide in the diagnosis and follow-up of sarcoid, has been used extensively in numerous clinical drug trials and is an outcome measure in sarcoid. [Remy-Jardin, 1994; Brauner, 1992; Greco, 2014; Erdal, 2014]

However, it typically relies on the anatomical depiction of fibrosis, characterised by traction bronchiectasis, reticulation and honeycombing. [Nishino, 2010; Criado, 2010]

Imaging modalities such as magnetic resonance imaging (MRI) have been used extensively in the investigation of fibrotic pulmonary sarcoid with varying degrees of success. [Cohen, 1987; McFadden, 1987, Craig, 1988; Mendelson, 1992; Gaeta, 2000; Lutterbey, 2005; Lutterbey, 2007; Chung, 2013]

There is no data concerning late enhancement regarding pulmonary lesions in sarcoidosis. [Tadamura, 2005]

6.2.2 Characterisation of lung fibrosis in IPF

Accurate depiction and quantification of pulmonary fibrosis on imaging is also important for diagnosis, treatment and prognosis in idiopathic pulmonary fibrosis. [Lynch, 2005; Raghu 2011]

Like sarcoidosis, the gold-standard non-invasive imaging test is chest CT, which is now widely utilised worldwide in the diagnosis and follow-up of IPF, in clinical drug trials and as an measure of outcome in IPF. [Raghu 2014; Raghu, 2012]

And like sarcoidosis, it also relies predominantly on the anatomical depiction of fibrosis , as previously described, as the hallmarks of pulmonary fibrosis. [Raghu, 2014; Souza, 2005]

Other imaging modalities, principally MRI, have also been used to depict pulmonary fibrosis with varying degrees of success. [Corteville, 2014; Rajaram, 2014; Ohno, 2013; Seki, 2014]

6.2.3 Rationale for late-enhanced contrast MRI

The advantages of MRI are its lack of ionising radiation and versatile tissue characterisation abilities, whilst its limitations relate principally to spatial resolution and contrast-to-noise ratios in depicting the lung parenchyma compared to high resolution computed tomography (HRCT). Although several non-contrast and contrast enhanced MRI protocols have been published to assess pulmonary fibrosis, none have acquired widespread acceptance in routine clinical practice. [Ackman, 2014]

Many studies have shown that a specific double-inversion recovery sequence, applied approximately 10 minutes after intravenous gadolinium administration, allows contrast to wash out of normal myocardium but remain concentrated within the myocardial fibrosis. [Simonetti, 2001]

The concentration of gadolinium within myocardial fibrosis relative to non-fibrotic myocardium relates to the increased extracellular space characterizing fibrotic tissue. [Kim, 2007] Since gadolinium is an extracellular contrast agent, it diffuses out of the blood pool and normal tissues and concentrates in tissues with an enlarged extracellular space.

Tissue characterisation by late-enhanced imaging has been principally used to detect myocardial infarction, but has subsequently proven to be valuable in depicting myocardial fibrosis in other cardiomyopathies. [O'Donnell, 2012]

We hypothesized that since late-enhancement MRI detects myocardial fibrosis because of its tissue histopathological characteristics, it might also be capable of detecting pulmonary fibrosis. The aim of this study was to compare a commonly used late-enhanced MRI tissue characterization sequence for the detection, localization and quantification of pulmonary fibrosis to the reference standard of HRCT anatomical characterisation of pulmonary fibrosis.

7 Materials and methods

7.1 Study 1: Assessment of fibrosis in pulmonary sarcoidosis using late-enhanced MR imaging

This section describes the methodology of the first study involving patients with fibrotic pulmonary sarcoid.

7.1.1 Patients

The imaging database was evaluated for patients (mean age = 67.3 +/- 9.4, range 40-79, 13 males) with documented clinical, radiological and histopathological features diagnostic of chronic fibrotic sarcoid based on ATS/ERS criteria. [Hunninghake, 1999] Patients were randomly chosen and invited to prospectively undergo lung function testing, HRCT and a late-enhanced MRI of thorax.

Patients were excluded if they developed symptoms and/or signs of an acute lower respiratory tract infection or acute exacerbation of sarcoid in the period between late-enhanced MRI, HRCT or lung function tests. Any patient with a contraindication to MRI or CT was also excluded.

Twelve control subjects with no lung disease were randomly recruited from our research database (mean age = 52.4 +/- 14.0, range 35-76, 6 males). A CHOYKE questionnaire was administered prior to all MR scans. Creatinine levels were

checked in those with a history of renal disease, renal stone, hypertension, gout, diabetes, proteinuria or prior kidney surgery. Demographic and clinical data was determined including details on the diagnosis, details of prior and current treatment, smoking status and quantification by pack years, and details of other lung conditions.

The study was performed with local institutional review board approval and written informed consent was obtained from all subjects.

7.1.2 CT Protocol

The HRCT scans was obtained on a Siemens Sensation 64-slice CT (Siemens, Erlangen, Germany) from apex to lung base at full inspiration using 120 kVP and 130 mAs. Contiguous slices were reconstructed at 1mm slice thickness with a 0.5mm increment using a high-spatial frequency edge-enhancing algorithm. Lung windows with a window width of 1500 and centre of -700 were applied to all images. No contrast was administered.

7.1.3 MRI Protocol

All subjects were examined on a 1.5 Tesla magnet (GE Healthcare, Milwaukee, Wis) using an eight-element phased-array cardiac coil (GE Healthcare, Aurora, Ohio) and peak gradient and slew rate. A stack of axial two-dimensional steady-state-free-precession images were acquired (FIESTA; GE Healthcare) using the following parameters: repetition time msec/echo time msec, 2.8/1.0; flip angle, 50°; field of view sized to individual patients; matrix, 256 3 256; bandwidth, 125 kHz; and section thickness, 8 mm. The lung apex to the diaphragm was covered in one breath hold at full inspiration and with a 12-16 second breath-hold. These were followed by a bolus injection of 0.2 mmol/kg of hand-injected gadoterate meglumine (Dotarem, Gd-DTPA – Guerbet, France).

Between 10-12 minutes later, three-dimensional late-enhanced MRI was obtained using a high-resolution, ECG-gated double inversion-recovery prepared fast-gradient echo pulse sequence in the axial image plane. [Simonetti, 2001; Knowles, 2014; Saranathan, 2004] Image slabs measured 2cm in the cranio-caudal direction. Between 4-6 slabs were acquired from the lung apex to the base. Voxel size was 1.25 x 1.25 x 5mm, TR/TE 5.5/2.3 ms, inversion time (TI) was between 230 to 310 ms, GRAPPA with speed-up factor of two, and 50 reference lines were acquired. The optimum TI value for each slab was identified using a scout scan of the main pulmonary artery and was chosen to minimize signal intensity of the pulmonary artery blood pool.

7.1.4 Image Analysis

All images were analysed in consensus by two blinded readers in random order. The MR images were read independent of the CT images. All images were read blind to the other imaging modality findings, clinical and demographic data.

The MRI scoring system for fibrotic pulmonary sarcoid was adapted from the scoring system by Desai et al. [Desai, 2004] Briefly, images were reviewed at five levels: 1. origin of the great vessels; 2. carina; 3. pulmonary venous confluence; 4. between levels 3 and 5; 5. 1cm above the right hemidiaphragm. Overall extent of interstitial lung disease was estimated to the nearest 5%. An assessment was then made of the relative proportions of interstitial lung disease (up to a total of 100%) made up of a reticular pattern, honeycombing and conglomerate fibrotic masses. The definitions of reticulation, honeycombing and conglomerate fibrotic masses were derived from the Fleischner society glossary of terms. [Hansell, 2008]

The reticulation was scored as fine (≤1mm) or thick (>1mm). Honeycombing was scored as either microcystic (≤4mm) or macrocystic (>4mm). An overall grade of

interstitial lung disease was also made depending on the relative extent of reticulation and honeycombing on the entire scan as follows: grade 1 - predominant reticular pattern, grade 2 – mixed pattern of reticulation and honeycombing pattern, grade 3 – predominantly honeycombing pattern and grade 4 – conglomerate fibrotic masses. For each patient, extent of fibrotic lung disease was derived by averaging the scores at each level. The overall coarseness score for each patient was derived by summing the scores at five levels (minimum score, 0; maximum score, 15). To prevent spurious reductions in the coarseness score, it was adjusted proportionately to a five-level score in patients with no disease in one or more slabs. A confidence score for pulmonary fibrosis was scored on a 5-point scale for each image slice (1-no fibrosis, 2-probably no fibrosis, 3-possible fibrosis, 4-probable fibrosis, 5-definite fibrosis). An identical approach was taken for scoring the lungs on HRCT. The overall confidence score for pulmonary fibrosis was derived by averaging the scores at all five levels to give a maximal potential score of 5. To prevent spurious reductions in disease extent scores were adjusted proportionately to a five level score in patients with no disease in one or more CT sections.

7.1.5 Late-enhancement MRI Analysis

The signal intensity of lung regions showing elevated signal were measured by placing three circular regions of interest (ROI's) in each area of elevated signal and the mean of the three readings were recorded. The ROI's were sized to avoid adjacent normal appearing lung. The signal intensity of normal appearing lung was also recorded using similar sized circular ROI's in areas of lung showing no evidence of elevated signal. The SD of image noise measured in a circular region of interest outside the body was also recorded.

The percent signal intensity elevation in the lung was calculated by using the following equation: 100 x (mean signal intensity of high signal intensity lung region - mean signal intensity of normal lung region)/(mean signal intensity of normal lung

region). Image contrast-to-noise ratios were calculated by using the following equation: (mean signal intensity of the lung region of elevated signal intensity - mean signal intensity of the remote region)/1.5 x (SD of noise).

7.1.6 Pulmonary function testing and dyspnoea assessment

Measurement of spirometry, lung volumes and diffusing capacity were performed by trained lung function technicians who were blinded to group assignment, according to American Thoracic Society/European Respiratory Society guidelines and standards. [Miller, 2005; MacIntyre, 2005] Predicted normal values were used to calculate percentage predicted values for forced expiratory volume in one second (FEV1), forced vital capacity (FVC), and single-breath carbon monoxide diffusing capacity of the lung (DLCO).

The Medical Research Dyspnoea scale was used to score dyspnoea (range 1-5) and was performed at the time of the MRI scan. [Mahler, 1988; Fletcher, 1959]

The St. George Respiratory Questionnaire (SGRQ) was also administered at the time of the MRI. This 76-item questionnaire is composed of three domains (symptoms, activity, and impact) as well as a total score. All four scores are normalised to a score range from 0 to 100, with a lower number correlating with a better health status. [Jones]

7.1.7 Statistical Analysis

Results are expressed as the mean ± SD and minimum and maximum range. Univariate correlations between MRI, HRCT and lung function were performed using Spearman rank correlation. Comparisons were performed with the independent t-test. Statistical calculations were performed using SPSS statistical software (version

13, SPSS Inc., Chicago, IL). A ‘P’ $< .05$ was considered significant for all calculations.

7.2 Study 2: Characterisation of lung fibrosis in idiopathic pulmonary fibrosis using late-enhanced MR imaging

This section describes the methodology of the second study involving patients with IPF. Much of the methodology is identical to that of Study 1, and thus not reiterated below.

7.2.1 Patients

The hospital database was evaluated for 20 patients (mean age = 67.3 $\pm$ 9.4, range 40-79, 13 males) with documented clinical and radiological features typical of IPF, based on ATS criteria. [ATS/ERS Consensus statement, 2010]

Patients were randomly chosen and invited to prospectively undergo spirometry, CT thorax and a late-enhanced MRI of thorax. No patients were current smokers. exclusion criteria were the same as those in Study1.

Twelve control subjects with no lung disease were randomly recruited from our research database (mean age = 53.4 $\pm$ 13.9, range 35-77, 6 males). Demographic and clinical data was determined including details on the diagnosis, details of prior and current treatment, smoking status and quantification by pack years, and details of other lung conditions.

The study was performed with local institutional review board approval and written informed consent was obtained from all patients.

7.2.2 CT Protocol

The CT protocol was identical to that described in Study 1.

7.2.3 MRI Protocol

The MRI protocol was identical to the protocol described in Study 1. Typical scan time was 15-20 minutes, depending on subject respiration and heart rate. In patients who required continuous O2 delivery during the examination, we applied a flexible nasal tube connected to the examination room O2 supply.

7.2.4 Image Analysis

All images were analysed in consensus by two blinded readers in random order. The MRI images were read independent of the CT images. All images were read blind to the other imaging modality findings, clinical and demographic data.

The MRI scoring system was the same that described in Study 1. Of note, conglomerate masses were not seen and thus not included in the overall grading of fibrosis.
A similar approach was taken for scoring the lungs on CT. Ground glass opacities were not included in the CT or MRI analysis as they were unlikely to be visualized on late-enhanced MRI.

7.2.5 Late-enhancement MRI Analysis

Regional signal intensity of normal lung, noise contrast ratios were measured in the same way as that described in Study 1.

7.2.6 Pulmonary function testing and dyspnoea assessment

Spirometric testing was carried out on each patient using standardized American Thoracic Society/European Respiratory Society methodology, [Miller, 2005] and dyspnoea scores were administered as described in Study 1.

7.2.7 Statistical Analysis

Results are expressed as the mean ± SD (range). Univariate correlations between MRI, CT and spirometry were performed using Spearman rank correlation. [Mukaka, 2012] Comparisons were performed with the independent t-test. Statistical calculations were performed using SPSS statistical software (version 13, SPSS Inc., Chicago, IL). A 'P' $< .05$ was considered significant for all calculations.

8 Results

8.1 Study 1

The next section describes the results of the first study involving patients with sarcoidosis.

8.1.1 Results

All scans were completed for all patients and there were no complications. There were no significant differences in age, gender or BMI between patients and controls (P = NS)(Table 1). Mean duration of disease from time of diagnosis was 180.8 ± 196.7 months (range 19-639 months). One patient was a current smoker and 10 were ex-smokers with a mean pack year history of 4.8 +/- 7.5 years. Three patients were not on active treatment, and the remainder was on a combination of steroids, cyclosporine and methotrexate. The mean Medical Research Dyspnoea scale score was 1.8 +/- 0.6, and the mean St. George's Respiratory Questionnaire score was 25.4 ± 15.4. A broad range of spirometric deficits was evident in FEV1 (2.5 +/- 1.0 L [range 1.3-4.7]) and FVC (3.7 +/- 1.2 L [range 1.9-5.5]) measurements. (Table 1)

High-resolution CT demonstrated a wide range of lung fibrosis severity, with a mean extent of fibrotic pulmonary sarcoid of 13.5% +/- 10.6 (range 1-41%). Sixty-eight percent (11 patients) of the fibrosis was characterised predominantly by reticulation (81.5% +/- 27.5), followed by conglomerate fibrotic masses (18.8%, 3 patients) and honeycombing (12.5%, two patients). The majority of coarseness of fibrosis scores

were consistent with coarse reticulation (11.3 +/- 5.3). Similarly, the majority of honeycombing scores were consistent with microcystic rather than macrocystic honeycombing (1.0 +/- 3.1). CT scans were scored very confidently for almost all lobes, with a mean confidence score of 4.9 +/- 0.4. No control patient was scored as having any areas of fibrosis.

Mean MRI scan time was 31.9 +/- 3.5 minutes (range 25-38). Mean heart rate during MRI scan acquisition was 70.2 +/- 11.1. Late-enhanced MRI correctly identified all patients with fibrotic pulmonary sarcoid and all controls (Fig. 1). Mean signal intensity of normal lung on late-enhanced MRI was significantly higher for sarcoid patients compared to controls (1.1 +/- 0.1 vs. 11.1 +/- 4.8, $P < 0.001$). Mean signal intensity of late-enhanced fibrotic lung was 46.3 +/- 36.2 (Figs. 2-4). This resulted in a percent elevation in MR signal intensity of fibrotic pulmonary sarcoid of 302.8% +/- 219.3 compared with the signal intensity of normal lung. The mean contrast-to-noise ratio was 59.9 +/- 107.6. (Table 2)

There was no overall difference in confidence scores on late-enhanced MRI between control and sarcoid subjects (4.6 +/- 0.5 vs 4.7 +/- 0.3, $P = 0.33$) or late-enhanced MRI and HRCT (4.7 +/- 0.3 vs. 4.9 +/- 0.4, $P = 0.23$).

Late-enhanced MRI correlated significantly with HRCT for the extent of fibrotic pulmonary sarcoid ($R = 0.84$, $P < 0.001$)(Table 3). It did not correlate significantly with the percentage of reticulation or honeycombing (P = NS for both). There was no significant correlation between late-enhanced MRI and HCRT for the coarseness of fibrosis or for microcystic versus macrocystic honeycombing (P = NS for both).

8.1.2 Tables

Table 1: Clinical Characteristics of the study population

Demographics	Controls (12)	Sarcoid (16)
Age (Years)	52.4 +/- 14.0	50.9 +/- 12.1
Gender	6M	11M
BMI (kg/m^2)	27.7 +/- 6.5	25.8 +/- 3.8
Spirometry (patients)		
FEV_1, absolute	-	2.5 +/- 1.0
FEV_1, % predicted	-	3.4 +/- 0.8
FVC, absolute	-	3.7 +/- 1.2
FVC, % predicted	-	4.4 +/- 1.0
FEV_1/FVC, % absolute	-	65.8 +/- 12.5
FEV_1/FVC, % predicted	-	77.9 +/- 3.2
DLCO %	-	65.6 +/- 13.4

Numbers in parenthesis indicate number of patients; FEV1-forced expiratory volume in one second; FVC-forced vital capacity; DLCO-single breath carbon monoxide diffusing capacity of lung; *-P<0.01

Table 2: Signal Characteristics of LE-MRI in the study cohort

MRI Signal Characteristics	Controls	Sarcoid	P Value
SI Outside the Body	9.3 +/- 1.4	12.7 +/- 4.9	NS
SI Normal Appearing Lung	1.1 +/- 0.1	11.1 +/- 2.0	<0.01
SI Late-enhanced Fibrotic Lung	0.0	46.3 +/- 36.2	-
% /\ F/N	-	302.8 +/- 219.3	-
Contrast-to-noise Ratio	-	59.9 +/- 107.6	-

SI-signal intensity; SD-standard deviation of signal intensity; %∧F/N-percent elevation in MR signal intensity of lung fibrosis compared with signal intensity of normal lung;

Table 3: Correlations between CT and LE-MRI for fibrosis characterisation

Fibrosis Characteristics	Controls (10)		Patients (20)		R Value
	CT	LE-MRI	CT	LE-MRI	
Presence of Fibrosis	0	0	16	16	
Overall Lung Fibrosis Extent	-	-	18.4 +/- 11.1	18.1 +/- 11.3	0.84*
Reticulation % of Fibrotic Lung	-	-	81.8 +/- 27.5	64.1 +/- 33.1	0.30
Honeycombing % of Fibrotic Lung	-	-	4.2 +/- 11.8	3.4 +/- 12.4	0.22

Note-* - $P < 0.001$; HRCT-high-resolution CT; LE-MRI-late-enhanced MRI;

8.1.3 Figures

Figure 11: 53-year-old control subject. (a) High-resolution CT shows normal lung parenchyma. (b) Late-enhanced MRI thorax shows normal homogenous low signal throughout the lungs with no contrast-enhancement.

(a)

(b)

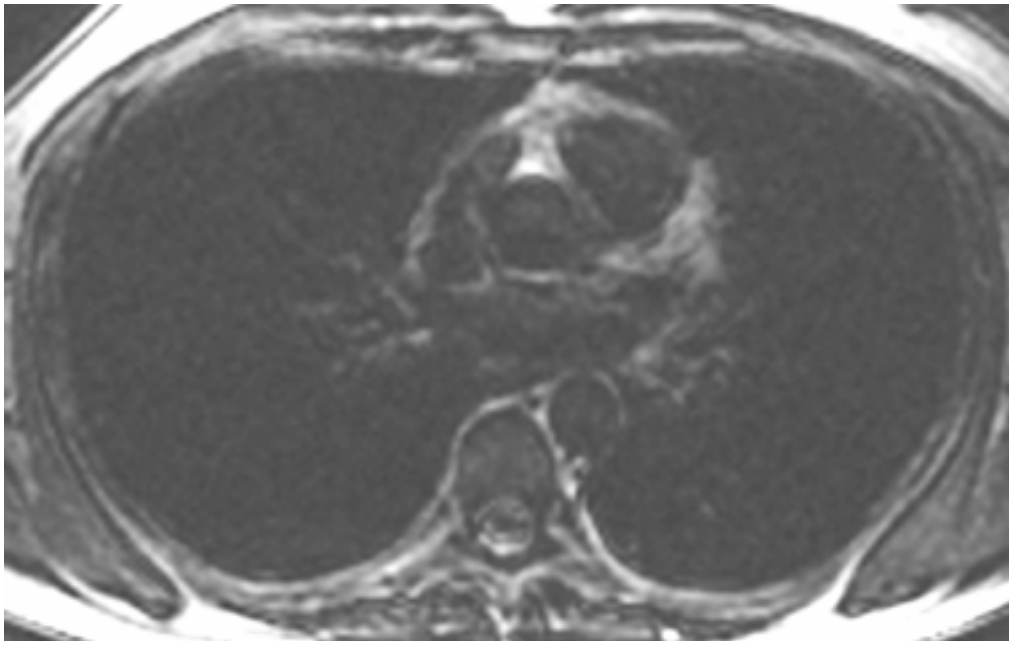

Figure 12: 63-year-man with moderate chronic fibrotic sarcoid. (a) High-resolution CT demonstrates asymmetric extensive bi-apical fibrosis in the upper lobes, worse in the left lung. (b) Late-enhanced MRI thorax shows extensive areas of late-enhancement (arrows) corresponding to the areas of fibrosis on HRCT. Traction bronchiectasis is clearly visible on the LE MRI thorax image.

(a)

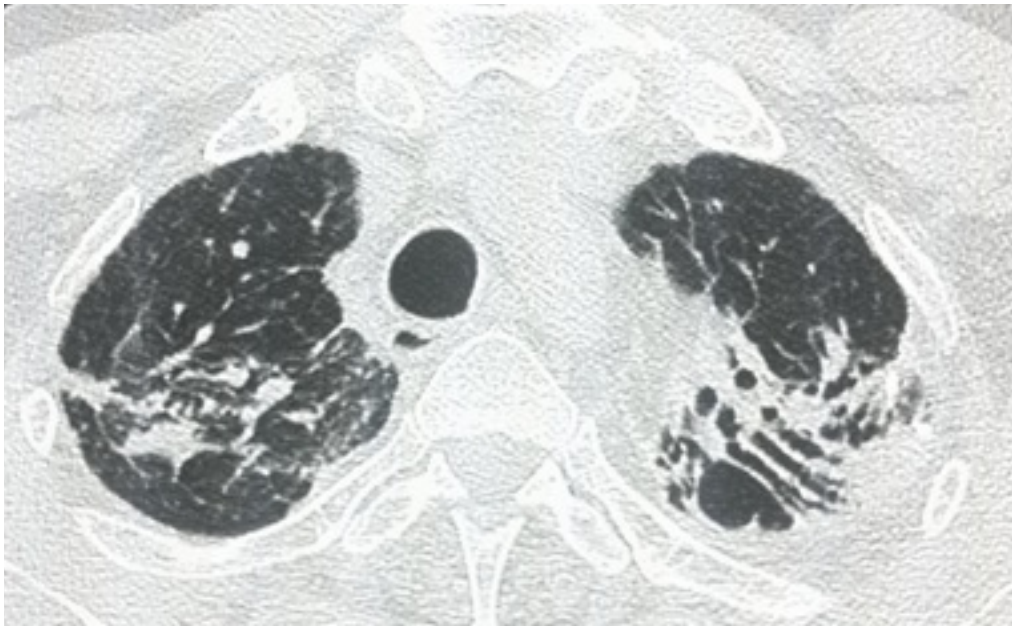

(b)

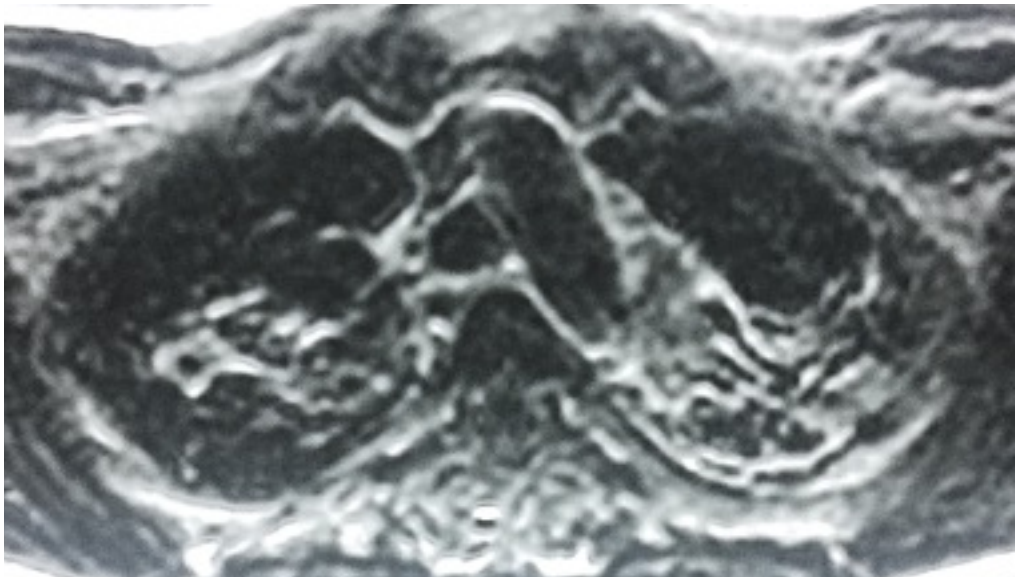

Figure 13: 58-year-old man with moderate fibrotic sarcoid. (a) High-resolution CT demonstrates conglomerate fibrotic masses in the upper lobes and areas of surrounding fibrosis. (b) Late-enhanced MRI thorax shows areas of LE within the conglomerate fibrotic masses corresponding to the appearances on HRCT.

(a)

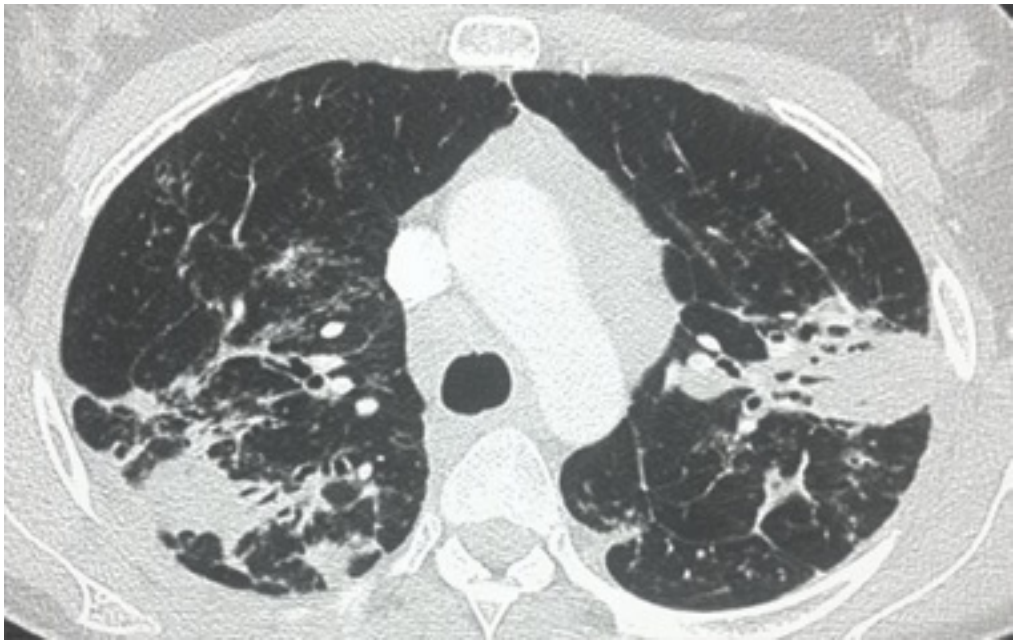

(b)

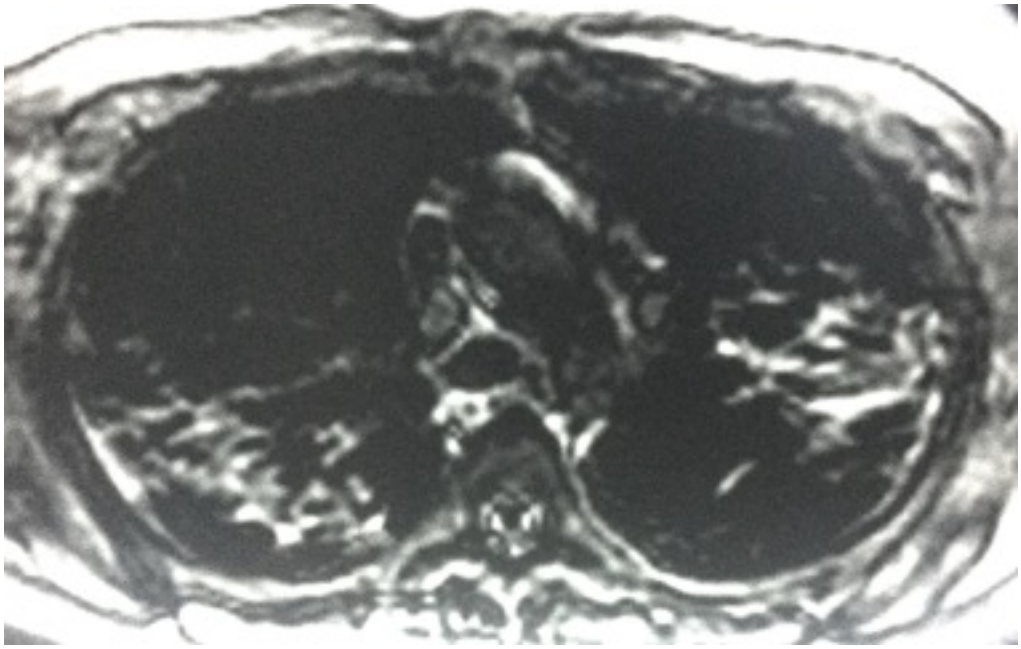

Figure 14: 56-year-old man with moderate diffuse chronic fibrotic pulmonary sarcoidosis. (a) HRCT shows extensive perihilar fibrosis and traction bronchiectasis. (b) LGE MRI thorax shows corresponding areas of LE with areas of traction bronchiectasis also identified.

(a)

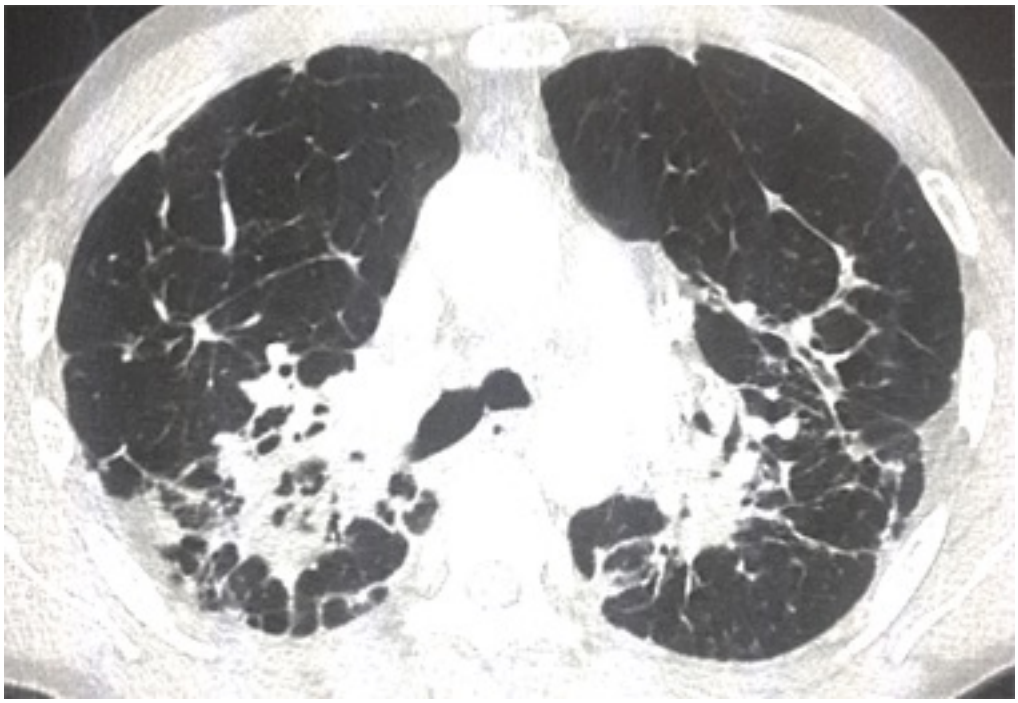

(b)

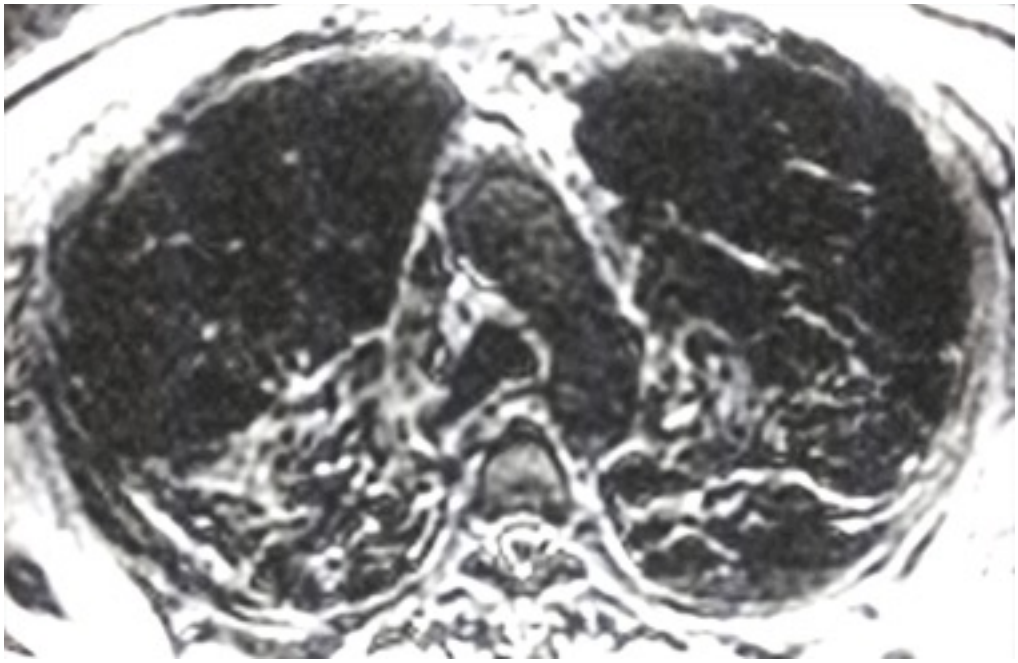

8.2 Study 2

The next section describes the results of the second study involving patients with IPF.

8.2.1 Results

All scans were completed for all patients and there were no complications, and no-one was lost to follow up. There were no significant differences in gender or BMI between patients and controls (P = NS) but the IPF group were significantly older (69.2 $\pm$ 9.2 vs 53.4 $\pm$ 13.4, P < 0.01)(Table 1). Mean duration of disease from time of diagnosis was 44 ± 36 months (range 3-123 months). No patients were current smokers but 12 were ex-smokers with a mean pack year history of 22. The mean Medical Research Dyspnoea scale score was 3.0 $\pm$ 1.5, and the mean St. George's Respiratory Questionnaire score was 49.7 ± 18.8 A broad range of spirometric deficits was evident in FEV1 (2.0 $\pm$ 0.5 L [range 1.2-2.7]) and FVC (2.5 $\pm$ 0.7 L [range 1.5-3.9]) measurements (Table 4).

CT demonstrated a mean extent of pulmonary fibrosis of 42% (range 14-68%). The majority of reticulation scores in all lobes were consistent with fine rather than coarse reticulation. Similarly, the majority of honeycombing scores were consistent with microcystic rather than macrocystic honeycombing. The mean percentage of reticulation was 33%. CT scans were scored very confidently for almost all lobes, with a mean confidence score of 4.8 $\pm$ 0.3 (range 4-5). No control patient showed any areas of fibrosis.

Mean MRI scan time was 32.8 $\pm$ 4.2 (range 25-40 minutes). Mean heart rate during MRI scan acquisition was 75.7 $\pm$ 11.3. Late-enhanced MRI correctly identified all

patients with pulmonary fibrosis and all controls (Fig. 1). Mean signal intensity of normal lung on late-enhanced MRI was significantly higher for IPF patients compared to controls (10.5 $\pm$ 1.6 vs. 8.5 $\pm$ 1.5, $P < 0.01$). Mean signal intensity of late-enhanced fibrotic lung was 31.8 $\pm$ 10.6 (Figs. 2-4). This resulted in a percent elevation in MR signal intensity of pulmonary fibrosis of 204.8% $\pm$ 90.6 compared with the signal intensity of normal lung. The mean MRI contrast-to-noise ratio was 22.8 $\pm$ 10.7. (Table 5)

There was no overall difference in confidence scores on late-enhanced MRI between control and IPF subjects (22.1 $\pm$ 2.9 vs 23.1 $\pm$ 2.4, P = NS). There were significant differences in confidence scores between late-enhanced MRI and CT (22.2 $\pm$ 2.8 vs. 24.3 $\pm$ 1.3, $P < 0.001$). (Table 6)

Late-enhanced MRI correlated significantly with CT for the extent of pulmonary fibrosis ($R = 0.78$, $P < 0.001$)(Table 3). It did not correlate significantly with the percentage of reticulation or honeycombing (P = NS for both). There was no significant correlation between late-enhanced MRI and CT for the coarseness of fibrosis or for microcystic versus macrocystic honeycombing (P = NS for both).

8.2.1 Tables

Table 4: Demographics of the study population

Demographics	Controls (12)	IPF (20)
Age (Years)	53.4 ± 13.9	69.2 ± 9.6*
Gender	6M /6F	13M / 7F
BMI (kg/m^2)	28.3 ± 6.3	27.9 ± 7.9
MRC score	0	3.0 $\pm$ 1.5
SGRQ score	-	49.7 ± 18.8
Spirometry (patients)		
FEV_1 (L), absolute		2.0 ± 0.5
FEV_1, % predicted		69.2 ± 12.2
FVC (L), absolute		2.5 ± 0.7
FVC, % predicted		61.7 ± 17.9
FEV_1/FVC (%)		81.3 ± 8.2

BMI = body mass index, FEV_1 = forced expiratory volume in one second,
FVC = forced vital capacity, MRC = medical research council, SGRQ = St. George's Respiratory Questionnaire; Numbers in parenthesis indicate number of patients; *P<0.01

Table 5: Signal Characteristics of LE-MRI in the study cohort

MRI Signal Characteristics	Controls	IPF	P Value
SD of SI Outside the Body	10.5 ± 0.6	11.8 ± 1.6	NS
SI Normal Appearing Lung	8.5 ± 1.5	10.5 ± 1.6	<0.01
SI Late-enhanced Fibrotic Lung	0.0	31.8 ± 10.6	-
% ∧ F/N	-	204.8 ± 90.6	-
Contrast-to-noise Ratio	-	22.8 ± 10.7	-

SD-standard deviation of signal intensity; IPF-idiopathic pulmonary fibrosis; %∧F/N-percent elevation in MR signal intensity of lung fibrosis compared with signal intensity of normal lung;

Table 6: Correlations between CT and LE-MRI for fibrosis characterisation

Fibrosis Characteristics	Controls (12)		Patients (20)		R Value
	CT	LE-MRI	CT	LE-MRI	
Presence of Fibrosis	0	0	20	20	
Overall Lung Fibrosis Extent	-	-	42.0 $\pm$ 15.7	42.1 $\pm$ 16.0	0.78*
Reticulation % of Fibrosis	-	-	25.8 $\pm$ 12.5	28.1 $\pm$ 11.8	0.30
Honeycombing % of Fibrosis	-	-	74.1 $\pm$ 12.5	70.7 $\pm$ 16.7	0.21

Note-* - $P < 0.001$; LE-MRI-late-enhanced MRI;

8.2.1 Tables

Figure 15: 53-year-old control subject with no respiratory history. (a) High-resolution CT shows normal lung parenchyma. (b) Late-enhanced MRI thorax shows normal homogenous low signal throughout the lungs with no contrast-enhancement.
(a)

(b)

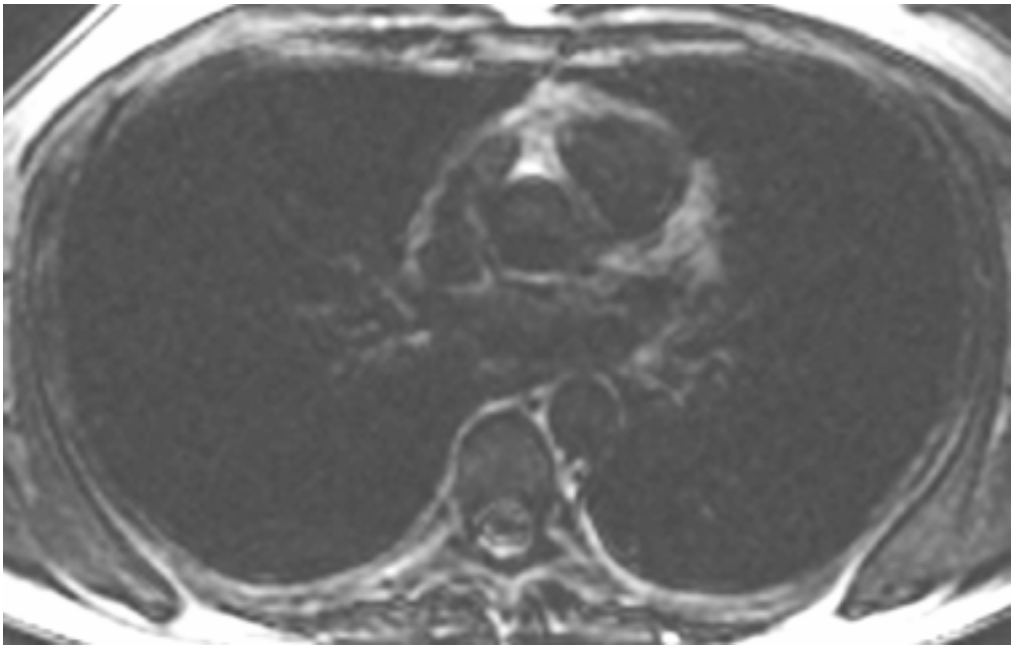

Figure 16: 75-year-man with moderate idiopathic pulmonary fibrosis. (a) CT demonstrates asymmetric extensive subpleural fibrosis (arrows) in the upper lobes, worse in the left upper lobe. (b) Late-enhanced MRI thorax shows extensive areas of late-enhancement (arrows) corresponding to the areas of fibrosis on CT. Note the ability to depict honeycombing and traction bronchiectasis in both upper lobes.

(a)

(b)

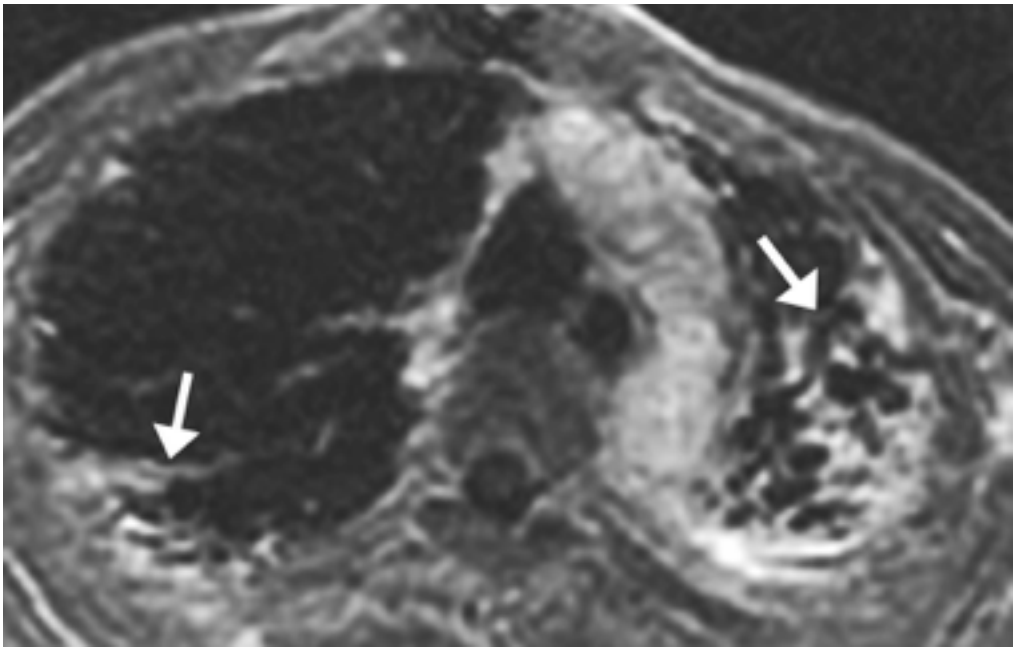

Figure 17: 58-year-old man with mild idiopathic pulmonary fibrosis. (a) CT demonstrates symmetric mild subpleural fibrosis (arrows) in the lower lobes, with microcystic honeycombing. (b) Late-enhanced MRI thorax shows areas of late-enhancement and subpleural microcystic honeycombing (arrows) corresponding to the appearances on CT.

(a)

(b)

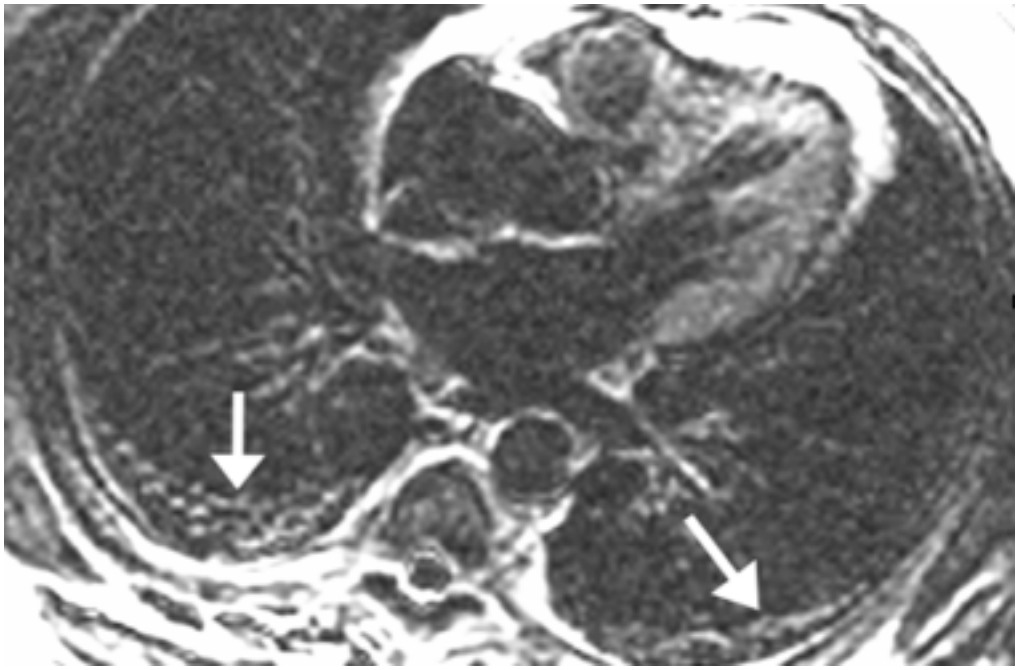

Figure 18: 40-year-old man with moderate idiopathic pulmonary fibrosis. (a) CT shows extensive macrocystic honeycombing throughout the left lower lobe (arrowheads). Less severe fibrotic changes are noted in the right lower lobe (arrowheads). (b) Late-enhanced MRI thorax shows corresponding extensive late-enhancement (arrowheads) throughout the lower lobes in keeping with diffuse fibrosis. Honeycombing is noted in the left lower lobe.

(a)

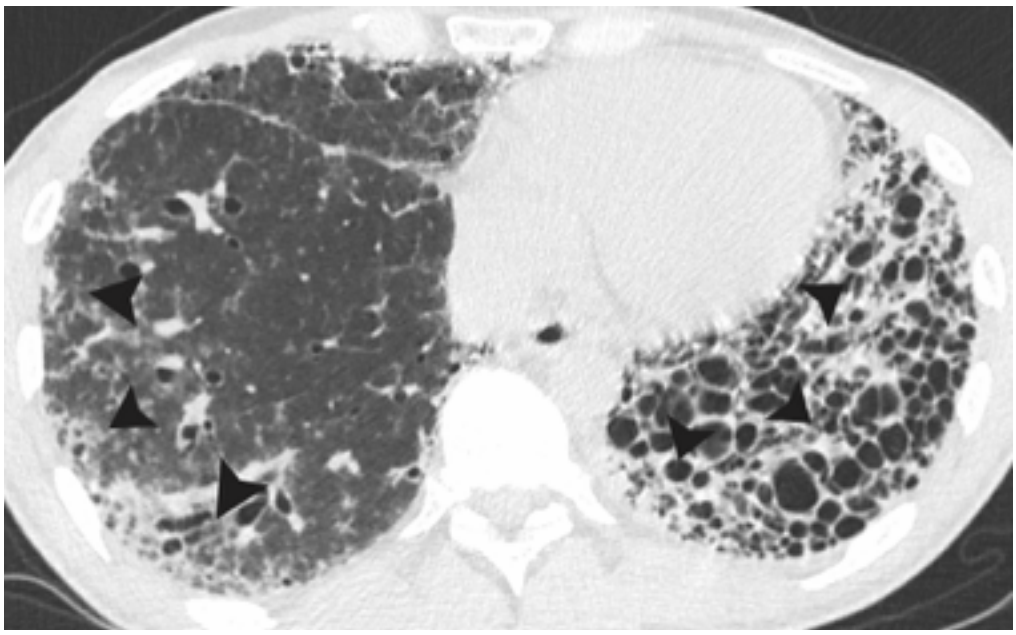

(b)

9 Discussion

The following sections discuss the results of the two studies

9.1 Study 1

The main findings from our study are that late-enhanced MRI using a specific segmented turboFLASH pulse sequence with a TI individually chosen to null the pulmonary arterial blood pool signal following contrast material administration produced significant differences in regional fibrotic pulmonary sarcoid compared with normal lung.

Gadolinium is an extracellular contrast agent, thus it concentrates in fibrotic tissue, which has an enlarged extracellular space relative to normal lung. This principle has been widely studied in many different types of cardiomyopathy. [Kim, 2008; O'Donnell, 2012] using gadolinium-based contrast agents. And since the fibrotic tissue in myocardium is histopathologically similar to lung fibrotic tissue, theoretically there is no reason why the cardiac MRI technique could not be applied to the detection of fibrotic pulmonary sarcoid.

The fibrotic process shares common fibrotic mesenchymal cells derived from the embryonic mesoderm tissue, and are not terminally differentiated. These can reactivate in many different organ systems through several chemical signals that

promote proliferation and cellular differentiation to form myofibroblasts with an up-regulated rate of matrix production. [Verecchia, 2007] Fibroblast over-activation becomes uncontrolled in entities such as IPF and cardiac fibrosis, producing a pathological fibrotic response. Fibroblast proliferation is particularly well validated in lung fibrosis using lineage-specific deletion of the type II transforming growth factor beta (TGFβ) receptor. [Hoyles, 2011] Transforming growth factor beta (TGFβ) receptor is also widely implicated in the increased expression of fibroblasts in cardiac fibrosis. [Euler-Taimor, 2006]

There are several important differences in applying the late-enhanced MRI technique between the heart and lungs. Firstly, late-enhancement MRI imaging of the myocardium relies on nulling normal myocardial tissue. When the normal myocardium is imaged at the correct inversion time or null time, it highlights fibrotic myocardium particularly well because the null time for normal myocardium differs by about 200 milliseconds from the null time of myocardial fibrosis. [Kim, 1999] In the lungs the late-enhancement of pulmonary fibrosis has a similar inversion time to that of the pulmonary blood pool (the difference is 40-60 milliseconds), and the use of a non-selective IR preparation pulse may actually suppress late-enhancement. Thus, the increased signal intensity from late-enhancement identified in pulmonary fibrosis tended not to be as strong as from myocardial fibrosis. Nonetheless, we found a mean percent elevation in MR signal intensity of lung fibrosis of 302.8% compared with the signal intensity of normal lung and a high contrast to noise ratio. The sequence requires a breath-hold of between 10-17 seconds, which is potentially problematic in dyspnoeic patients. Several techniques to achieve longer breath-holds such as supplemental oxygen, patient hyperventilating for 15-20 seconds before sequence acquisition and reducing the number of phase encoding steps of the sequence increase the ability to acquire the sequence without breathing artifacts. The use of three-dimensional sequencing to capture the lung with no slice gaps improves the in-plane spatial resolution, but it is theoretically possible to only use two-dimensional sequence, resulting in shorter breath-holds and potentially improving image quality as they are less sensitive to motion artifact. There would be

slice gaps and the requirement for many slices to adequately cover the lungs (approximately 12-15), ultimately resulting in a longer scan time and more frequent breath-holds.

We made a few useful observations during our study when applying the late-enhancement cardiac MRI sequence to the lungs. Sarcoid proved a more suitable fibrotic lung disease than IPF (Study 2) because the fibrosis tends to be more coarse. Thin septal lines <1mm in thickness can be difficult to visualize in IPF using this technique. This meant that in our sarcoid patients we were unable to differentiate reticulation from honeycombing.

Several papers have assessed the use of late-enhanced imaging to depict pulmonary fibrosis. King et al. used a spin-echo sequence to depict usual interstitial pneumonitis (UIP) imaged at 5-15 minutes post-contrast, but the sequence had insufficient sensitivity in detection for routine application because of breathing artifacts. [King, 1996] Gaeta et al. imaged 25 patients with interstitial lung disease at 1 and 3 minutes after contrast injection, and found early enhancement in inflammatory lesions but not in fibrosis. [Gaeta, 2000] Yi et al. investigated the use of dynamic contrast imaging in patients with UIP. They performed contrast imaging at 1,3 5 and 10 minutes using a dynamic T1-weighted 3D multishot turbo field-echo sequence and found early enhancement to predict inflammation-predominant lesions. However, only 41% of patients with fibrosis demonstrated late-enhancement, and the differences were not statistically different. [Yi, 2008]

Important additions in our approach were the use of individual inversion times to null the pulmonary blood pool and the lack of fat suppression to reduce sequence acquisition time. Chung et al were the first group to systematically compare CT to MR in pulmonary sarcoidosis, using a multi sequence approach (VIBE, HASTE, TrueFISP, BLADE). The post contrast VIBE images were taken 60-90 sec after contrast injection. They concluded that MR and CT showed good agreement. There was a weaker correlation for small nodules and fine reticulation owing to the inherent

lower spatial resolution of MR. There was also poorer agreement in the lower lobes, perhaps explained by motion artifact. [Chung, 2013]

Our findings have several potential clinical applications in sarcoid. Demonstrating late-enhancement in areas of abnormal appearing lung may assist in differentiating fibrosis from mimics such as emphysema. [Watadani, 2013] Although we specifically excluded patients with active sarcoid in this study, it would be interesting to compare this group to those with chronic fibrotic lung disease.

Our study has several limitations. First, our study was a feasibility study, and much work is needed to optimise the sequence further as it applies to pulmonary fibrosis, and to apply the sequence to a larger group of patients. We did not test the optimum delay time for performing the sequence, using 10 minutes because that is what is well established for myocardial fibrosis imaging, but it may be more advantageous to wait a longer time period before imaging for pulmonary fibrosis. This would allow further wash-out of contrast from the pulmonary blood pool while persisting in areas of pulmonary fibrosis. Finally, we did not compare the late-enhancement MRI sequence to potentially useful anatomical MRI sequences such as SSFP sequences, as our focus was on tissue characterisation rather than anatomical depiction.

9.2 Study 2

The main findings from our study are that late-enhanced MRI using a specific segmented turboFLASH pulse sequence with a T1 set to null the pulmonary arterial blood pool signal following contrast material administration produced significant differences in regional pulmonary fibrosis MR image signal intensity compared with normal lung.

Since gadolinium is an extracellular contrast agent, it concentrates in the enlarged extracellular space within fibrotic tissue, while being washed out of normal lung, thus allowing the detection of pulmonary fibrosis. The principle of detecting gadolinium-based contrast agents in fibrotic myocardial tissue has been extensively evaluated, and the technique is now widely applied to many different types of cardiomyopathy. [Kim, 2008; O'Donnell, 2012]

The fibrotic tissue in myocardium is similar histopathologically to lung fibrotic tissue, thus cardiac MRI technique could theoretically be applied to the detection of pulmonary fibrosis. There are, however, some important differences between the two organ systems. Firstly, late-enhancement MRI imaging of the myocardium relies on nulling normal myocardial tissue. When the normal myocardium is imaged at the correct inversion time or null time, it highlights fibrotic myocardium particularly well because the null time for normal myocardium differs by about 200 milliseconds from the null time of myocardial fibrosis. [Kim, 1999] Late-enhancement of pulmonary fibrosis has a similar inversion time to that of the pulmonary blood pool (the difference is 40-60 milliseconds), and the use of a non-selective IR preparation pulse may actually suppress late-enhancement. Thus, the increased signal intensity from late-enhancement identified in pulmonary fibrosis is not as strong as it is from myocardial fibrosis. Nonetheless, we found a 204.7% mean percent elevation in the

MR signal intensity of lung fibrosis compared with the signal intensity of normal lung and a high contrast to noise ratio.

The sequence does require a breath-hold of between 10-17 seconds, which can be problematic in patients with IPF. We used various techniques to obtain longer breath-holds such as administering supplemental oxygen via nasal prongs, or hyperventilating the patient for 15-20 seconds before sequence acquisition and reducing the number of phase encoding steps of the sequence, with the disadvantage of a reduction in spatial resolution. Furthermore, we used a three-dimensional sequence to capture the lung with no slice gaps, but it is theoretically possible to only use two-dimensional slice capture, which would result in shorter breath-holds and potentially improve image quality because they are less sensitive to motion artifact. The disadvantage is that there would be slice gaps and the requirement for many slices to adequately cover the lungs (approximately 12-15), ultimately resulting in a longer scan time and more frequent breath-holds.

Some notable practical observations were made during our study when applying the late-enhancement cardiac MRI sequence to the lungs. First, despite the excellent spatial resolution of the 3D late-enhanced sequence, thin septal lines <1mm in thickness were at times difficult to identify, and we were unable to accurately differentiate thin reticulation from honeycombing in some lung regions. Second, the normal central airway walls clearly showed late-enhancement using this technique and care was needed to avoid misinterpreting them as subpleural fibrosis adjacent to the hila. We noted considerable difficulty in differentiating bullae from macrocystic honeycombing. The late-enhanced sequence may require combination with an anatomical sequence such as an SSFP sequence to assist in differentiating such abnormalities from honeycombing.

Although to our knowledge we are the first to apply a double inversion ECG-gated sequence with specific pulmonary blood pool nulling for the tissue characterisation of pulmonary fibrosis, others have used gadolinium-enhanced MRI to depict pulmonary

fibrosis. Three papers used late-enhanced imaging to depict pulmonary fibrosis. King et al. used a spin-echo sequence to depict usual interstitial pneumonitis (UIP) imaged at 5-15 minutes post-contrast, [King, 1996] but the sequence had insufficient sensitivity in detection for routine application because of breathing artifacts. Gaeta et al. imaged 25 patients with interstitial lung disease at 1 and 3 minutes after contrast injection, and found early enhancement in inflammatory lesions but not in fibrosis. [Gaeta, 2000] Yi et al. investigated the use of dynamic contrast imaging in patients with UIP. [Yi, 2008] They performed contrast imaging at 1,3, 5 and 10 minutes using a dynamic T1-weighted 3D multishot turbo field-echo sequence in an attempt to differentiate areas of active inflammation from fibrotic lesions whose patterns overlapped on CT imaging, and found early enhancement to predict inflammation-predominant lesions and although late-enhancement to in their study was not statistically predictive of pulmonary fibrosis. Important additions in our approach were the use of individual inversion times to null the pulmonary blood pool and the lack of fat suppression reducing sequence acquisition time.

Our findings have several potential applications. Demonstrating late-enhancement in areas of abnormal appearing lung may assist in differentiating fibrosis from mimickers such as emphysema. [Lynch, 2005; Watadani, 2013] This might be of particular value in patients with combined pulmonary emphysema-fibrosis syndrome, to evaluate the percentage of abnormal lung that is fibrotic. [Akira, 2009] Another difficulty when interpreting HRCT from an anatomical perspective relates to differentiating honeycombing from infection superimposed on emphysema, which can have similar imaging appearances. Further studies are needed to elucidate whether late-enhanced MRI of the lungs can play a useful role in these contexts.

Our study has several limitations. First, our study was a feasibility study, and much work is needed to optimize the sequence further as it applies to pulmonary fibrosis, and to apply the sequence to a larger group of patients. Our control group were younger, which was statistically significant, however this difference is unlikely to have substantially influenced our findings, since older patients without IPF rarely

show honeycombing. We did not test the optimum delay time for performing the sequence, using 10 minutes because that is what is well established for myocardial fibrosis imaging, but it may be more advantageous to wait a longer time period before imaging for pulmonary fibrosis. This would allow further wash-out of contrast from the pulmonary blood pool while persisting in areas of pulmonary fibrosis. We did not compare the late-enhancement MRI sequence to potentially useful anatomical MRI sequences such as SSFP sequences, and further studies could be done to perform this comparison. Finally, we did not have surgical confirmation of IPF. We deliberately chose cases that were absolutely classical of IPF (definite), with typical clinical and imaging findings. We felt this was appropriate since current recommendations support such a non-invasive approach in typical cases. Nevertheless, it would be useful to have histopathological confirmation of our hypothesis in at least one case.

9 Conclusions

Based on the two studies presented we can conclude that a late-enhanced MRI thorax with individual nulling of the pulmonary blood pool signal allows us to detect and quantify the extent of pulmonary fibrosis, and compares accurately to the anatomical characterisation of pulmonary fibrosis on high-resolution chest CT in both fibrotic pulmonary sarcoidosis and patients with idiopathic pulmonary fibrosis.

10 Summary

This work presents the use of a specific sequence borrowed from cardiac MRI, and used here to image fibrosis in the lung.

The main contribution of this work is the addition of a late-enhancement contrast sequence based on tissue characterization rather than anatomical depiction of fibrosis in two specific patient populations with pulmonary fibrosis.

But given that pulmonary fibrosis is a final common pathway, [Noble, 2002] it is likely that the sequence would be useful in other etiologies of pulmonary fibrosis.

Our work shows that MRI remains inferior to CT in terms of spatial resolution.

However its ability to depict certain tissues, in this case pulmonary fibrosis, may give specific sequences that take advantage of this tissue characterisation a role in the longtitudinal evaluation of patients with pulmonary fibrosis, reducing risk attributable to ionising radiation.

More work is needed to optimise the spatial resolution and thus sensitivity of thoracic MRI, as well as improvements in specific contrast imaging markers linked to gadolinium that might bind to fibrotic receptors, thus increasing the specificity of imaging in these disorders.

11 Bibliography

1. Ackman JB, Wu CC, Halpern EF, Abbott GF, Shepard J-AO. Nonvascular thoracic magnetic resonance imaging: the current state of training, utilization, and perceived value: survey of the society of thoracic radiology membership. J Thorac Imaging. 2014;29(4):252–257.

2. Akira M, Inoue Y, Kitaichi M, Yamamoto S, Arai T, Toyokawa K. Usual interstitial pneumonia and nonspecific interstitial pneumonia with and without concurrent emphysema: thin-section CT findings. Radiology. 2009;251(1):271-279.

3. American Thoracic Society, European Respiratory Society. Idiopathic pulmonary fibrosis: diagnosis and treatment. International consensus statement. Am J Respir Crit Care Med. 2000;161:646–664.

4. Arakawa H, Johkoh T, Honma K, Saito Y, Fukushima Y, Shida H, et al. Chronic interstitial pneumonia in silicosis and mix-dust pneumoconiosis: its prevalence and comparison of CT findings with idiopathic pulmonary fibrosis. Chest. 2007;131(6):1870–1876.

5. Bader TR, Semelka RC, Pedro MS, Armao DM, Brown MA, Molina PL. Magnetic resonance imaging of pulmonary parenchymal disease using a modified breath-hold 3D gradient-echo technique: initial observations. J Magn Reson Imaging. 2002;15:31–38.

6. Balan A, E.T.D. Hoey ETD, Sheerin F, Lakkaraju A, Chowdhury FU. Multi-technique imaging of sarcoidosis. Clin Radiol. 2010;65(9):750-760.

7. Bannier E, Cieslar K, Mosbah K, Aubert F, Duboeuf F, Salhi Z, Gaillard S, Berthezène Y, Crémillieux Y, Reix P. Hyperpolarized 3He MR for Sensitive Imaging of Ventilation

Function and Treatment Efficiency in Young Cystic Fibrosis Patients with Normal Lung Function. Radiology. 2010;255: 225-232.

8. Baughman RP, Shipley R, Desai S, Drent M, Judson MA, Costabel U, du Bois RM, Kavuru M, Schlenker-Herceg R, Flavin S, et al. Changes in chest roentgenogram of sarcoidosis patients during a clinical trial of infliximab therapy: comparison of different methods of evaluation. Chest. 2009;136:526–535.

9. Baughman RP, Sparkman BK, Lower EE. Six-Minute Walk Test and Health Status Assessment in Sarcoidosis. Chest. 2007;132(1):207-213.

10. Baughman RP, Culver DA, Judson MA. A concise review of pulmonary sarcoidosis. Am J Respir Crit Care Med. 2011;183(5):573-581.

11. Baughman RP, Lower EE. The effect of corticosteroid or methotrexate therapy on lung lymphocytes and macrophages in sarcoidosis. The American Review of respiratory Disease.
1990;142(6 Pt. 1):1268-1271.

12. Baughman RP, Nunes H. Therapy for sarcoidosis: evidence-based recommendations. Expert Rev Clin Immunol. 2012;8(1):95-103.

13. Bauman G, Johnson KM, Bell LC, Velikina JV, Samsonov AA, Nagle SK. Three-dimensional pulmonary perfusion MRI with radial ultrashort echo time and spatial-temporal constrained reconstruction. Magn Reson Med. 2014 Mar 6. doi: 10.1002/mrm. 25158. [Epub ahead of print]

14. Bernstein MA, King KF, Zhou XJ. Handbook of MRI pulse sequences. 1st edition, Academic Press, 2004.

15. Berthezene Y, Vexler V, Kuwatsuru R, et al. Differentiation of alveolitis and pulmonary fibrosis with a macromolecular MR imaging contrast agent. Radiology. 1992;185:97–103.

16. Biederer J, Reuter M, Both M, Muhle C, Grimm J, Graessner J, Heller M. Analysis of artefacts and detail resolution of lung MRI with breath-hold T1-weighted gradient-echo

and T2-weighted fast spin-echo sequences with respiratory triggering. Eur Radiol. 2002;12(2):378-384.

17. Biederer J. General Requirements of MRI of the Lung and Suggest Standard Protocol. MRI of the Lung. 2010; ISBN 978-3-642-0799-7.

18. Biederer J, Reuter M, Both M, et al. Analysis of artifacts and detail resolution of lung MRI with breath-hold T1 weighted gradient-echo and T2 weighted fast spin-echo sequences with respiratory triggering. Eur Radiol. 2002;12:378–384.

19. Biederer J, Hintze C, Fabel M. MRI of pulmonary nodules: technique and diagnostic value. Cancer Imaging. 2008;8:125–130.

20. Biederer J, Both M, Graessner J, Carsten Liess C, Jakob P, Reuter M, Heller M. Lung Morphology: Fast MR Imaging Assessment with a Volumetric Interpolated Breath-Hold Technique: Initial Experience with Patients. Radiology. 2003; 226:242–249.

21. Biederer, J, Hintze C, Fabel M, Dinkel J . Magnetic resonance imaging and computed tomography of respiratory mechanics. Magn. Reson. Imaging. 2010;32:1388–1397.

22. Biederer J, Heussel CP, Puderbach M, Wielpuetz MO. Functional magnetic resonance imaging of the lung. Semin Respir Crit Care Med. 2014;35(1):74-82.

23. Bilsky MH, Vitaz TW, Boland PJ, Bains MS, Rajaraman V, Rusch VW. Surgical treatment of superior sulcus tumors with spinal and brachial plexus involvement. J Neurosurg. 2002;97(3 Suppl):301-309.

24. Bitar R, Leung G, Perng R, Tadros S, Moody AR, Sarrazin J, et al. MR Pulse Sequences: What Every Radiologist Wants to Know but Is Afraid to Ask. RadioGraphics. 2006;26:513–537.

25. Bloch F, Hansen WW, Packard ME. Nuclear induction. Phys Rev. 1946;69:127.

26. Both M, Schultze J, Reuter M, et al. Fast T1- and T2-weighted pulmonary MR-imaging in patients with bronchial carcinoma. Eur J Radiol. 2005;53:478–488.

27. Bottomley PA, Hardy CJ, Argersinger RE, Allenmoore G. A review of H-1 nuclear-magnetic-resonance relaxation in pathology - are T1 and T2 diagnostic. Med Phys. 1987;14:1–37.

28. Brauner MW. Lenoir S. Grenier P. Cluzel P. Battesti J. Valeyre D. Pulmonary sarcoidosis: CT assessment of lesion reversibility. Radiology. 1992:182:349-354.

29. Brown MA, Semelka RC. MRI: basic principles and applications. 3rd edition, John Wiley and Sons Inc, 2003.

30. Bruegel M, Gaa J, Woertler K, Waldt S, Hillerer C, Rummeny EJ. MRI of the lung: value of different turbo spin-echo, single- shot turbo spin-echo, and 3D gradient- echo pulse sequences for the detection of pulmonary metastases. J Magn Reson Imaging. 2007;25:73–81.

31. Bydder GM, Young IR. MR imaging: clinical use of the inversion recovery sequence. JCAT.1985;9:659-675.

32. Caravan P, Das B, Dumas S, Epstein FH, Helm PA, Jacques V, Koerner S, Kolodziej A, Shen L, Sun WC, and Zhang Z. Collagen-Targeted MRI Contrast Agent for Molecular Imaging of Fibrosis. Angew. Chem. Int. Ed. 2007;46:8171–8173.

33. Carr HY. Steady-state free precession in nuclear magnetic resonance. Phys Rev. 1958;112:1693–1701.

34. Chang, JA, Curtis, JR, Patrick, DL, et al Assessment of health-related quality of life in patients with interstitial lung disease. Chest. 1999;116:1175-1182.

35. Chen DL, Kinahan PE. Multimodality molecular imaging of the lung. J Magn Reson Imaging. 2010;32(6):1409-1420.

36. Chung JH, Little BP, Forssen AV, Yong J, Nambu A, Kazlouski D Puderbach M, Biederer J, Lynch DA. Proton MRI in the evaluation of pulmonary sarcoidosis: Comparison to chest CT. European Journal of Radiology. 2013; 82: 2378–2385.

37.Cohen MD, Scales RL, Eigen H, Scott P, Tepper R, Cory DA, Smith JA. Evaluation of pulmonary parenchymal disease by magnetic resonance imaging. Br J Radiol. 1987;60(711):223-230.

38.Coolen J, Vansteenkiste J, De Keyzer F, Decaluwé H, De Wever W, Deroose C. Characterisation of solitary pulmonary lesions combining visual perfusion and quantitative diffusion MR imaging. Eur Radiol. 2014;24(2):531-541.

39.Corteville DMR, Kjørstad A, Henzler T, Zöllner FG, Schad LR. Fourier decomposition pulmonary MRI using a variable flip angle balanced steady-state free precession technique. Magn Reson Med. 2014 May 20.

40.Cottin V. Changing the idiopathic pulmonary fibrosis treatment approach and improving patient outcomes. Eur Respir Rev. 2012;21(124):161-167.

41.Couch MJ, Ball IK, Lib T, Fox MS, Ouriadov AV, Biman B, Alberta MS. Inert fluorinated gas MRI: a new pulmonary imaging modality. NMR Biomed. 2014; 27: 1525–1534.

42.Craig DA, Colletti PM, Ratto D, Gordonson JS, Raval JK, Sharma OP. MRI findings in pulmonary sarcoidosis. Magn Reson Imaging. 1988;6(5):567-573.

43.Criando E, Sánchez M, Ramírez J, de Caralt PAP, TM, Perea RJ, Xaubet A. Pulmonary Sarcoidosis: Typical and Atypical Manifestations at High- Resolution CT with Pathologic Correlation. RadioGraphics. 2010; 30:1567–1586.

44.Cronin P, Dwamena BA, Kelly AM, et al: Solitary pulmonary nodules and masses: A meta-analysis of the diagnostic utility of alternative imaging tests. Eur Radiol. 2008;18:1840-1856.

45.Damadian R. Tumor Detection by Nuclear Magnetic Resonance. Science. 1971:171(3976):1151-1153.

46.De Coene B, Hajnal JV, Gatehouse P, et al. MR of the brain using fluid-attenuated inversion recovery (FLAIR) pulse sequences. AJNR Am J Neuroradiol. 1992;13:1555–1564.

47. Desai SR, Veeraraghavan S, Hansell DM, Nikolakopolou A, Goh NS, Nicholson AG, et al. CT features of lung disease in patients with systemic sclerosis: comparison with idiopathic pulmonary fibrosis and nonspecific interstitial pneumonia. Radiology. 2004;232(2):560–567.

48. Deshmane A, Gulani V, Griswold MA, Seiberlich N. Parallel MR imaging. J Magn Reson Imaging. 2012;36(1):55-72.

49. Diederich et al. Screening for asymptomatic early bronchogenic carcinoma with low dose CT of the chest. Cancer 2000; 89(11 Suppl):2483–2484.

50. Dregely I, Mugler III JP, Ruset JC, Altes TA, Mata JF, Miller GW, Ketel J, Ketel S, Distelbrink J, Hersman FW, Ruppert K. Hyperpolarized Xenon-129 Gas-Exchange Imaging of Lung Microstructure: First Case Studies in Subjects With Obstructive Lung Disease. J. Magn. Reson. Imaging. 2011;33:1052–1062.

51. Dothager RS, Piwnica-Worms D. Molecular imaging of pulmonary disease in vivo. Proc Am Thorac Soc. 2009;6(5):403-410.

52. du Bois RM. Corticosteroids in sarcoidosis: friend or foe? Eur Respir J. 1994;7:1203–1209.

53. du Bois RM. An earlier and more confident diagnosis of idiopathic pulmonary fibrosis. Eur Respir Rev. 2012;21(124):141-146.

54. Edelman RR, Chien D, Kim D. Fast selective black blood MR imaging. Radiology. 1991;181(3):655–660.

55. Eichinger M, Heussel CP, Kauczor HU, Tiddens H, Puderbach M. Computed tomography and magnetic resonance imaging in cystic fibrosis lung disease. J Magn Reson Imaging. 2010;32(6):1370-1378.

56. Emami K, Xu Y, Hamedani H, Profka H, Kadlecek S, Xin Y, Ishii M, Rizi RR. Accelerated Fractional Ventilation Imaging with Hyperpolarized Gas MRI. Magn Reson Med. 2013;70(5): . doi:10.1002/mrm.24582.

57.Erdal BS, Crouser ED, Yildiz V, King MA, Patterson AT, at al. Quantitative computerized two-point correlation analysis of lung CT scans correlates with pulmonary function in pulmonary sarcoidosis. Chest. 2012;142(6):1589-1597.

58. Ernst RR, Bodenhausen G, Wokaun A. Principles of nuclear magnetic resonance in one and two dimensions. Oxford: Clarendon; 1987. p 125–148.

59. Euler-Taimor G, Heger J. The complex pattern of SMAD signaling in the cardiovascular system. Cardiovasc. Res. 2006;69(1):15–25.

60. Fain S, Schiebler ML, McCormack DG, Parraga G .Imaging of Lung Function Using Hyperpolarized Helium-3 Magnetic Resonance Imaging: Review of Current and Emerging Translational Methods and Applications. J. Magn. Reson. Imaging. 2010;32:1398–1408.

61. Fain S, Panth SR, Evans MD, Wentland AL, Holmes JH, Korosec FR, O'Brien MJ, Fountaine H, Grist TM. Early Emphysematous Changes in Asymptomatic Smokers: Detection with 3He MR Imaging. Radiology. 2006; 239:875-883.

62.Fain S, Schiebler ML, McCormack DG, Parraga G. Imaging of lung function using hyperpolarized helium-3 magnetic resonance imaging: Review of current and emerging translational methods and applications. J. Magn. Reson. Imaging. 2010;32:1398–1408.

63.Fan L, Sher A, Kohan A, Vercher-Conejero J, Rajiah P. PET/MRI in Lung Cancer. Semin Roentgenol. 2014;49(4):291-303.

64.Feinberg DA, Hale JD, Watts JC, Kaufman L, Mark A. Halving MR imaging time by conjugation: demonstration at 3.5 kG. Radiology. 1986;161:537.

65.Fink C, Puderbach M, Biederer J, Fabel M, Dietrich O, Kauczor HU, Reiser MF, Schönberg SO. Lung MRI at 1.5 and 3 Tesla: observer preference study and lesion contrast using five different pulse sequences. Invest Radiol. 2007;42:377–383.

66.Fletcher CM, Elmes PC, Fairbairn AS, et al. The significance of respiratory symptoms and the diagnosis of chronic bronchitis in a working population. BMJ 1959; 2:257–266.

67.Froehlich JM. MR Contrast Agents. How does MRI work? Second edition, Springer, Berlin Heidelberg New York 2006.

68. Gaeta M, Blandino A, Scribano E, et al. Chronic infiltrative lung diseases: value of gadolinium- enhanced MRI in the evaluation of disease activity—early report. Chest. 2000; 117:1173–1178.

69. Gallagher TA, Nemeth, AJ, Hacein-Bey L. An Introduction to the Fourier Transform: Relationship to MRI. AJR. 2008;190:1396–1405.

70. Gorkem SB, Coskun A, Yikilmaz A, Zurakowski D, Mulkern RV, Lee EY. Evaluation of pediatric thoracic disorders: comparison of unenhanced fast-imaging-sequence 1.5-T MRI and contrast-enhanced MDCT. AJR Am J Roentgenol. 2013;200(6):1352-1357.

71. Greco FG, Spagnolo P, Muri M, Paladini I, Chizzolini F, et al. The value of chest radiograph and computed tomography in pulmonary sarcoidosis. Sarcoidosis Vasc Diffuse Lung Dis. 2014;31(2):108-116.

72. Griswold MA, Jakob PM, Heidemann RM, Nittka M, Jellus V, Wang J, Kiefer B, Haase A. Generalized auto-calibrating partially parallel acquisitions (GRAPPA). Magn Reson Med. 2002;47(6):1202–1210.

73. Günther A, Korfei M, Mahavadi P, von der Beck D, Ruppert C, Markart P. Unravelling the progressive pathophysiology of idiopathic pulmonary fibrosis.Eur Respir Rev. 2012;21(124):152-160.

74. Haacke EM,Brown RW,Thompson MR,Venkatesan R. Magnetic resonance imaging: physical principles and sequence design. New York: John Wiley and Sons; 1999.

75. Habersberger J, Manins V, Taylor AJ. Cardiac sarcoidosis. Intern Med J. 2008;38:270-277.

76. Hahn EL. Spin echoes. Phys Rev. 1950;80:580–594.

77. Hansell DM, Bankier AA, MacMahon H, McLoud TC, Muller NL, Remy J. Fleischner Society: glossary of terms for thoracic imaging. Radiology. 2008;246(3):697–722.

78. Hansen MS, Kellman P. Image reconstruction: An overview for clinicians. J Magn Reson Imaging. 2014 Jun 25. doi: 10.1002/jmri.24687. [Epub ahead of print]

79. Hanson LG. Is Quantum Mechanics necessary for understanding Magnetic Resonance? Concepts in Magnetic Resonance. 2008;32A(5):329-340.

80. Hashemi RH,Bradley WG, Lisanti C. MRI: the basics. 3rd edition, Lippincott, Williams & Wilkins, 2010.

81. Hatubu H, Gaa J, Tadamura E, Edinburgh KJ, Stock KW, Garpestad E, Edelman RR. MR imaging of pulmonary parenchyma with a half-Fourier single-shot turbo spin-echo (HASTE) sequence. European Journal of Radiology. 1999;29:152–159.

82. Hatabu H, Gaa J, Kim D, Li W, Prasad PV, Edelman RR. Pulmonary perfusion: qualitative assessment with dynamic contrast-enhanced MRI using ultra-short TE and inversion recovery turbo FLASH. Magn Reson Med. 1996;36(4):503-508.

83. Helm E, Matin TN, Gleeson FV. Imaging of the pleura. J. Magn. Reson. Imaging. 2010;32:1275–1286.

84. Henkelman RM, Stanisz GJ, Graham SJ. Magnetization transfer in review. NMR Biomed. 2001;14:57–64.

85. Henzler T, Dietrich O, Krissak R, Wichmann T, Lanz T, Reiser MF, Schoenberg SO, Fink C. Half-Fourier-acquisition single-shot turbo spin-echo (HASTE) MRI of the lung at 3 Tesla using parallel imaging with 32-receiver channel technology. J Magn Reson Imaging. 2009;30(3):541-546.

86. Hopkins S, Prisk GK. Lung perfusion measured using magnetic resonance imaging: New tools for physiological insights into the pulmonary circulation. J. Magn. Reson. Imaging. 2010;32:1287–1301.

87. Heidemann RM, Griswold MA, Kiefer B, Nittka M, Wang J, Jellus V, Jakob PM. Resolution enhancement in lung 1H imaging using parallel imaging methods. Magn Reson Med. 2003;49:391–394.

88. Hekimoglu K, Sancak T, Tor M, Besir H, Kalaycıoglu B, Gündogdu S. Fast MRI evaluation of pulmonary progressive massive fibrosis with VIBE and HASTE sequences: comparison with CT. Diagn Interv Radiol. 2010;16(1):30-37.

89. Hennig J. Echoes-How to Generate, Recognize, Use or Avoid Them in MR-Imaging Sequences Part I: Fundamental and Not So Fundamental Properties of Spin Echoes. Concepts in Magnetic Resonance. 1991;3:125-143.

90. Hennig J. Echoes-How to Generate, Recognize, Use or Avoid Them in MR-Imaging Sequences Part I: Echoes in imaging sequences. Concepts in Magnetic Resonance. 1991;3:179-192.

91. Henzler T, Schmid-Bindert G, Schoenberg SO, Fink C. Diffusion and perfusion MRI of the lung and mediastinum. Eur J Radiol. 2010;76(3):329-336.

92. Heye T, Ley S, Heussel CP, Dienemann H, Kauczor HU, Hosch W, Libicher M. Detection and size of pulmonary lesions: how accurate is MRI? A prospective comparison of CT and MRI. Acta Radiol. 2012;53(2):153-160.

93. Hochhegger B, Marchiori E, Irion K, Moreira J, Zanetti G. MRI in assessment of lung cancer. Thorax. 2011;66(4):357.

94. Hornak JP. The basics of MRI. 2014. http://www.cis.rit.edu/htbooks/mri/

95. Hoyles RK, Derrett-Smith EC, Khan K, Shiwen X, Howat SL, Wells AU, et al. An essential role for resident fibroblasts in experimental lung fibrosis is defined by lineage-specific deletion of high-affinity type II transforming growth factor β receptor. Am. J. Respir. Crit. Care Med. 2011;183(2):249–261.

96. Huber AM, Schoenberg SO, Hayes C, Spannagl B, Engelmann MG, Franz WM, Reiser MF. Phase-sensitive inversion-recovery MR imaging in the detection of myocardial infarction. Radiology. 2005;237(3):854-860.

97. Hunninghake et al. ATS/ERS/ WASOG statement on sarcoidosis. American Thoracic Society/ European Respiratory Society/World Association of Sarcoidosis and other Granulomatous Disorders. AJRCCM. 1999;160(2):736-755.

98. Iannuzzi M, Rybicki BA, Teirstein AS. Sarcoidosis. N Engl J Med. 2007;357:2153-2165.

99.Jacob RE, Amidan BG, Soelberg J, Minard KR. In Vivo MRI of Altered Proton Signal Intensity and T2 Relaxation in a Bleomycin Model of Pulmonary Inflammation and Fibrosis. J. Magn. Reson. Imaging. 2010;31:1091–1099.

100.Jones, PW, Quirk, FH, Baveystock, CM, et al A self-complete measure of health status for chronic airflow limitation: the St. George's Respiratory Questionnaire. Am Rev Respir Dis. 1992;145:1321-1327.

101.Judson MA, Gilbert GE, Rodgers JK, Greer CF, Schabel SI. The utility of the chest radiograph in diagnosing exacerbations of pulmonary sarcoidosis. Respirology. 2008;13:97–102.

102.Judson MA. The treatment of pulmonary sarcoidosis. Respiratory Medicine. 2012;106:1351-1361.

103.Jung BA, Weigel M. Spin Echo Magnetic Resonance Imaging. J. Magn. Reson. Imaging. 2013;37:805–817.

104.Jung JI, Park SH, Lee JM, Hahn ST, Kim KA. MR characteristics of progressive massive fibrosis. J Thorac Imaging. 2000;15:144-150.

105.Kadlecek S, Hamedani H, Xu Y, Emami K, Xin Y, Ishii M, Rizi R. Regional alveolar partial pressure of oxygen measurement with parallel accelerated hyperpolarized gas MRI. Acad Radiol. 2013;20(10):1224-1233.

106.Karabulut N, Martin DR, Yang M, Tallaksen RJ. MR Imaging of the chest using a contrast-enhanced breath-hold modified three-dimensional gradient-echo technique: comparison with two-dimensional gradient-echo technique and multidetector CT. AJR Am J Roentgenol. 2002; 179:1225-1233.

107.Kauczor HU, Kreitner KF. MRI of the pulmonary parenchyma. Eur Radiol. 1999; 9:1755-1764.

108.Kauppinen RA, Peet AC. Using magnetic resonance imaging and spectroscopy in cancer diagnostics and monitoring: Preclinical and clinical approaches. Cancer Biology & Therapy. 2011;12(8):665-679.

109.Keil B, Wald LL. Massively Parallel MRI Detector Arrays. Magn Reson. 2013;229:75–89.

110.Keijsers RG, Grutters JC, Thomeer M, Du Bois RM, Van Buul MM, Lavalaye J, Van Den Bosch JM, Verzijlbergen FJ. Imaging the inflammatory activity of sarcoidosis: sensitivity and inter observer agreement of (67)Ga imaging and (18)F-FDG PET. Q J Nucl Med Mol Imag. 2011;55:66-71.

111.Kellman P, Arai AE. Cardiac imaging techniques for physicians: late enhancement. J Magn Reson Imaging. 2012;36(3):529-542.

112.King TE, Bradford WZ, Castro-Bernardini S, Fagan EA, Glaspole I, Glassberg MK, et al. A Phase 3 Trial of Pirfenidone in Patients with Idiopathic Pulmonary Fibrosis. N Engl J Med. 2014;370:2083-2092.

113.King M, Bergin C, Ghadishah E, Yi E, Clark J. Detecting pulmonary abnormalities on magnetic resonance images in patients with usual interstitial pneumonitis: effects of varying window settings and gadopentetate dimeglumine. Acad Radiol. 1996;3:300–307.

114.Kim RJ, Albert TS, Wible JH, Elliott MD, Allen JC, Lee JC, et al. Performance of delayed-enhancement magnetic resonance imaging with gadoversetamide contrast for the detection and assessment of myocardial infarction: an international, multicenter, double-blinded, randomized trial. Circulation. 2008;117(5):629–637.

115.Kim RJ, Wu E, Rafael A, Chen EL, Parker MA, Simonetti O, et al. The use of contrast-enhanced magnetic resonance imaging to identify reversible myocardial dysfunction. N Engl J Med. 2000;343(20):1445–1453.

116.Kim RJ, Fieno DS, Parrish TB, Harris K, Chen EL, Simonetti O, et al. Relationship of MRI delayed contrast enhancement to irreversible injury, infarct age, and contractile function. Circulation. 1999;100(19):1992–2002.

117.Kim RJ, Shah DJ, Judd RM. How we perform delayed enhancement imaging. J Cardiovasc Magn Reson. 2003;5(3):505–514.

118.Kim RJ. Cardiovascular MRI. W B Saunders Company; 2007.

119.King MA, Bergin CJ, Ghadishah E, Yi ES, Clark JB. Detecting pulmonary abnormalities on magnetic resonance images in patients with usual interstitial pneumonitis: effect of varying window settings and gadopentetate dimeglumine. Acad Radiol. 1996;3(4):300–307.

120.Kistler KD, Nalysnyk L, Rotella P, Esser D. Lung transplantation in idiopathic pulmonary fibrosis: a systematic review of the literature. BMC Pulmonary Medicine. 2014;14:139.

121.Kluge A, Luboldt W, Bachmann G. Acute Pulmonary Embolism to the Subsegmental Level: Diagnostic Accuracy of Three MRI Techniques Compared with 16-MDCT. AJR. 2006; 187:W7–W14.

122.Knowles BR, Peters DC, Clough RE, Razavi R, Schaeffter T, Prieto C. Three-dimensional late gadolinium-enhanced mr imaging of the left atrium: a comparison of spiral versus Cartesian k-space trajectories. J Magn Reson Imaging. 2014;39(1):211–216.

123.Koyama T, Ueda H, Togashi K, Umeoka S, Kataoka M, Nagai S. Radiologic manifestations of sarcoidosis in various organs. RadioGraphics. 2004; 24:87–104.

124.Kumar A, Welti D, Ernst RR. NMR Fourier zeugmatography. J Magn Res. 1975;18:69-83.

125.Lauterbur PC. Magnetic resonance zeugmatography. Pure and Applied Chemistry. 1974;40:149-157.

126.Lauterbur PC. Image formation by induced local interactions: examples of employing nuclear magnetic resonance. Nature. 1973;242:190-191.

127.Leung AN, Brauner MW, Caillat-Vigneron N, Valeyre D, Grenier P. Sarcoidosis activity: correlation of HRCT findings with those of 67Ga scanning, bronchoalveolar lavage, and serum angiotensin-converting enzyme assay. J Comput Assist Tomogr. 1998; 22: 229–234.

128.Leutner C, Gieseke J, Lutterbey G, Kuhl CK, Flacke S, Glasmacher A et al. (1999) MRI versus CT in the diagnosis of pneumonias: an evaluation of a T2-weighted ultrafast turbo-spin-echo sequence (UTSE). Rofo 170:449–456.

129.Ley-Zaporozhan J, van Beek EJ. Imaging phenotypes of chronic obstructive pulmonary disease. J Magn Reson Imaging. 2010;32(6):1340-1352.

130.Ley S, Grünig E, Kiely DG, Edwin van Beek, Wild J. Computed tomography and magnetic resonance imaging of pulmonary hypertension: Pulmonary vessels and right ventricle. J. Magn. Reson. Imaging. 2010;32:1313–1324.

131.Ley B, Collard HR, King TE Jr. Clinical course and prediction of survival in idiopathic pulmonary fibrosis. Am J Respir Crit Care Med. 2011;183(4):431-440.

132.Liszewski MC, Hersman FW, Altes TA, Ohno Y, Ciet P, Warfield SK. Magnetic resonance imaging of pediatric lung parenchyma, airways, vasculature, ventilation, and perfusion: state of the art. Radiol Clin North Am. 2013 Jul;51(4):555-82.

133.Lutterbey G, Grohé C, Gieseke J, et al. Initial experience with lung-MRI at 3.0T: Comparison with CT and clinical data in the evaluation of interstitial lung disease activity. Eur J Radiol. 2007;61(2):256-261.

134.Lutterbey G, Gieseke J, von Falkenhausen M, Morakkabati N, Schild H. Lung MRI at 3.0 T: a comparison of helical CT and high-field MRI in the detection of diffuse lung disease. Eur Radiol. 2005; 15:324–328.

135.Lynch DA, Godwin JD, Safrin S, Starko KM, Hormel P, Brown KK, et al. High-resolution computed tomography in idiopathic pulmonary fibrosis: diagnosis and prognosis. Am. J. Respir. Crit. Care Med. 2005;172(4):488–493.

136.Mahler DA, Wells CK: Evaluation of clinical methods for rating dyspnea. Chest 1988, 93:580–586.

137.Markl M, Leupold J. Gradient Echo Imaging. J. Magn. Reson. Imaging. 2012;35:1274–1289.

138.Matsumoto S, Miyake H, Oga M, Takaki H, Mori H. Diagnosis of lung cancer in a patient with pneumoconiosis and progressive massive fibrosis using MRI. Eur Radiol. 1998; 8:615–617.

139.McFadden RG, Carr TJ, Wood TE. Proton magnetic resonance imaging to stage activity of interstitial lung disease. Chest. 1987;92(1):31-39.

140.McGee KP, Mariappan YK, Hubmayr RD, Carter RE, Bao Z, Levin DL, Manduca A, Ehman RL. Magnetic resonance assessment of parenchymal elasticity in normal and edematous, ventilator-injured lung. J Appl Physiol. 2012;113(4):666-676.

141.Meltzer EB, Noble PW. Idiopathic pulmonary fibrosis. Orphanet J Rare Dis. 2008; 3:8.

142.Mendelson DS, Gray CE, Teirstein AS. Magnetic resonance findings in sarcoidosis of the thorax. Magn Reson Imaging. 1992;10:523–529.

143.MacIntyre N, Crapo RO, Viegi G, Johnson DC, van der Grinten CPM, et al. Standardisation of the single-breath determination of carbon monoxide uptake in the lung. Eur Respir J 2005; 26: 720–735.

144.Miller MR, Hankinson J, Brusasco V, Burgos F, Casaburi R, Coates A, et al. Standardisation of spirometry. Eur Respir J. 2005;26(2):319-338.

145.Millera GW, Mugler JP, Sác RC, Altesa TA, Prisk GK, Hopkins SR. Advances in functional and structural imaging of the human lung using proton MRI. NMR Biomed. 2014;27:1542-1556.

146.Mukaka MM. Statistics Corner: A guide to appropriate use of Correlation coefficient in medical research. Malawi Medical Journal. 2012;24(3):69-71.

147.Muller N et al. Value of MR imaging in the evaluation of chronic infiltrative lung diseases: comparison with CT. AJR. 1992;158(6):1205-1209.

148.Nagai T, Kohsaka S, Okuda S, Anzai T, Asano K, Fukuda K. Incidence and Prognostic Significance of Myocardial Late Gadolinium-Enhancement in Sarcoidosis Patients without Cardiac Manifestation. Chest. 2014 May 22. doi: 10.1378/chest.14-0139. [Epub ahead of print]

149.Nishimura K, Itoh H, Kitaichi M, Nagai S, Izumi T. Pulmonary sarcoidosis: correlation of CT and histopathologic findings. Radiology. 1993;189(1):105–109.

150.Nishino M, Lee KS, Itoh H, Hatabu H. The spectrum of pulmonary sarcoidosis: variations of high-resolution CT findings and clues for specific diagnosis. European Journal of Radiology 2010:73(1):66–73.

151.Noble PW, Barkauskas CE, Jiang D. Pulmonary fibrosis: patterns and perpetrators. J Clin Invest. 2012;122(8):2756-2762.

152.Noël P, Bammer R, Reinhold C, Haider MA. Parallel Imaging Artifacts in Body Magnetic Resonance Imaging. Can Assoc Radiol J. 2009;60(2):91–98.

153.Nunes et al. Imaging in sarcoidosis. Semin Respir Crit Care Med. 2007;28:102–120.

154.O'Donnell DH, Abbara S, Chaithiraphan V, Yared K, Killeen RP, Martos R, et al. Cardiac MR imaging of nonischemic cardiomyopathies: imaging protocols and spectra of appearances. Radiology. 2012 Feb;262(2):403–422.

155.Ohba et al. Diffusion-weighted magnetic resonance for pulmonary nodules: 1.5 vs. 3 Tesla. Asian Cardiovasc Thorac Ann. 2011;19(2):108-114.

156.O h-Ici D, Ridgway JP, Kuehne T, Berger F, Plein S, Sivananthan M, Messroghli DR. Cardiovascular magnetic resonance of myocardial edema using a short inversion time inversion recovery (STIR) black-blood technique: diagnostic accuracy of visual and semi-quantitative assessment. J Cardiovasc Magn Reson. 2012;14:22.

157.Ohira H, Tsujino I, Ishimaru S, Oyama N, Takei T, Tsukamoto E, et al.Myocardial imaging with 18F-fluoro-2-deoxyglucose positron emission tomography and magnetic resonance imaging in sarcoidosis. Eur J Nucl Med Mol Imaging Springer. 2008;35:933–941.

158.Ohno Y, Hatabu H, Takenaka D, Adachi S, Van Cauteren M, Sugimura K. Oxygen-enhanced MR ventilation imaging of the lung: preliminary clinical experience in 25 subjects. AJR. 2001;177(1):185-194.

159.Ohno Y, Koyama H, Matsumoto K, Onishi Y, Nogami M, Takenaka D, Yoshikawa T, Matsumoto S, Sugimura K. Dynamic MR perfusion imaging: Capability for quantitative assessment of disease extent and prediction of outcome for patients with acute pulmonary thromboembolism. J. Magn. Reson. Imaging 2010;31:1081–1090.

160.Ohno et al. Solitary Pulmonary Nodules: Potential Role of Dynamic MR Imaging in Management—Initial Experience. Radiology 2002; 224:503–511.

161.Ohno et al. Pulmonary magnetic resonance imaging for airway diseases. J Thorac Imaging. 2011;26(4):301-316.

162.Ohno Y, Nishioa M, Koyamac H, Yoshikawa T, Sumiaki Matsumoto S, et al. Comparison of the utility of whole-body MRI with and without contrast-enhanced Quick 3D and double RF fat suppression techniques, conventional whole-body MRI, PET/CT and conventional examination for assessment of recurrence in NSCLC patients. EJR. 2013;82:2018–2027.

163.Ohno Y, Nishio M, Koyama H, Takenaka D, Takahashi M, Yoshikawa T, et al. Pulmonary MR imaging with ultra-short TEs: utility for disease severity assessment of connective tissue disease patients. Eur J Radiol. 2013;82(8):1359–1365.

164.Ohno Y, Hatabu H, Takenaka D, et al: Metastases in mediastinal and hilar lymph nodes in patients with non–small cell lung cancer: Quantitative and qualitative assessment with STIR turbo spin-echo MR imaging. Radiology. 2004;231:872-879.

165.Oppelt A, Graumann R, Barfuss H, et al. FISP—a new fast MRI sequence. Electromedica. 1986;54:15-18.

166.Ordovas KG, Higgins CB. Delayed contrast enhancement on MR images of myocardium: past, present, future. Radiology. 2011;261(2):358-374.

167.I. Herráez Ortega HI, López González L. Update thoracic sarcoidosis. Radiología. 2011;53(5):434-448.

168.Paramothayan NS, Lasserson TJ, Jones PW. Corticosteroids for pulmonary sarcoidosis. Cochrane Database Syst Rev. 2005; CD001114.

169. Paramothayan S, Lasserson T, Walters EH. Immunosuppressive and cytotoxic therapy for pulmonary sarcoidosis. Cochrane Database Syst Rev. 2003;CD003536.

170. Paschal CB, Morris DH. K-Space in the Clinic. J. Magn. Reson. Imaging. 2004;19:145–159.

171. Pauls et al. The role of dynamic, contrast-enhanced MRI in differentiating lung tumor subtypes. Clin Imaging. 2011;35(4):259-265.

172. Pipe, JG, Motion correction with PROPELLER MRI: Application to head motion and free-breathing cardiac imaging. Magnetic Resonance Medicine. 1999;42:963–969.

173. Plewes DB, Kucharczyk W. Physics of MRI: A Primer. J. Magn. Reson. Imaging. 2012;35:1038–1054.

174. Pooley RA. Fundamental Physics of MR Imaging. RadioGraphics. 2005;25:1087–1099.

175. Prabhakar HB, Rabinowitz CB, Gibbons FK, O'Donnell WJ, Shepard JA, Aquino SL. Imaging features of sarcoidosis on MDCT, FDG PET, and PET/CT. AJR Am J Roentgenol. 2008;190(3 Suppl):S1-6.

176. Primack SL, Mayo JR, Hartman TE, Miller RR, Müller NL. MRI of infiltrative lung disease: comparison with pathologic findings. J Comput Assist Tomogr. 1994;18(2): 233-238.

177. Pruessmann KP, Weiger M, Scheidegger MB, Boesiger P. SENSE: sensitivity encoding for fast MRI. Magn Reson Med. 1999;42(5):952–962.

178. Puderbach et al.The role of advanced imaging techniques in cystic fibrosis follow-up: is there a place for MRI? Pediatr Radiol. 2010;40(6):844-849.

179. Puderbach M, Eichinger M, Haeselbarth J, et al. Assessment of morphological MRI for pulmonary changes in cystic fibrosis (CF) patients: comparison to thin-section CT and chest x-ray. Invest Radiol. 2007;42:715–725.

180. Puderbach M, Eichinger M, Gahr J, Ley S, Tuengerthal S, Schmähl A, Fink C, Plathow C, Wiebel M, Müller FM, Kauczor HU. Proton MRI appearance of cystic fibrosis: comparison to CT. Eur Radiol. 2007;17(3):716-724.

181. Rabi II, Zacharias JR, Millman S, Kusch P. A new method of measuring nuclear magnetic moment. Phys Rev.1938;53:318.

182. Rajaram S, Swift AJ, Capener D, Telfer A, Davies C, Hill C, Condliffe R, Elliot C, Hurdman J, Kiely DG, Wild JM. Lung morphology assessment with balanced steady-state free precession MR imaging compared with CT. Radiology. 2012; 263(2): 569-577.

183. Raghu G, Collard HR, Egan JJ, et al. An Official ATS/ERS/JRS/ ALAT statement: Idiopathic pulmonary fibrosis: evidence-based guidelines for diagnosis and management. Am J Respir Crit Care Med. 2011;183: 788–824.

184. Raghu G, Lynch D, Godwin JD, Webb R, Colby TV, Leslie KO, et al. Diagnosis of idiopathic pulmonary fibrosis with high-resolution CT in patients with little or no radiological evidence of honeycombing: secondary analysis of a randomised, controlled trial. Lancet Respir Med. 2014;2(4):277–284.

185. Raghu G. Idiopathic pulmonary fibrosis: new evidence and an improved standard of care in 2012. Lancet. 2012;380(9842):699–701.

186. Ramsey NF. Early history of Magnetic Resonance. Phys. Perspective. 1999;1(2): 123-135.

187. Redpath TW, Smith FW. Technical note: Use of a double inversion recovery pulse sequence to image selectively grey or white brain matter. The British Journal of Radiology. 1994;67:1258-1263.

188. Remy-Jardin M, Giraud F, Remy J, Wattinne L, Wallaert B, Duhamel A. Pulmonary sarcoidosis: role of CT in the evaluation of disease activity and functional impairment and in prognosis assessment. Radiology. 1994;191:675–680.

189. Richeldi L, du Bois RM, Raghu G, Azuma A, Brown KK, Costabel U, et al. Efficacy and safety of nintedanib in idiopathic pulmonary fibrosis. N Engl J Med. 2014;370(22): 2071-2082.

190. Ridgway JP. Cardiovascular magnetic resonance physics for clinicians: part I Journal of Cardiovascular Magnetic Resonance. 2010;12:71.

191. Rofsky NM, Lee VS, Laub G, et al. Abdominal MR imaging with a volumetric interpolated breath-hold examination. Radiology. 1999;212:876–884.

192. Rohren EM, Provenzale JM, Barboriak DP, et al: Screening for cerebral metastases with FDG PET in patients undergoing whole-body staging of non-central nervous system malignancy. Radiology. 2003;226:181-187.

193. Santos MK, Elias J Jr, Mauad FM, Muglia VF, Trad CS. Magnetic resonance imaging of the chest: current and new applications, with an emphasis on pulmonology. J Bras Pneumol. 2011;37(2):242-258.

194. Saranathan M, Rochitte CE, Foo TKF. Fast, three-dimensional free-breathing MR imaging of myocardial infarction: a feasibility study. Magn Reson Med. 2004;51(5):1055–1060.

195. Satoh S, Nakaminato S, Kihara A, Isogai S, and Kawai S. Evaluation of Indeterminate Pulmonary Nodules with Dynamic MR Imaging. Magn Reson Med Sci. 2013; 12(1):31–38.

196. Scadding JG. Prognosis of intrathoracic sarcoidosis in England. A review of 136 cases after five years' observation. Br Med J. 1961;2(5261):1165-1172.

197. Scheffler K, Lehnhardt S. Principles and applications of balanced SSFP techniques. Eur Radiol. 2003;13(11):2409-18.

198. Schroeder T, Ruehm SG, Debatin JF, Ladd ME, Barkhausen J, Goehde SC. Detection of pulmonary nodules using a 2D HASTE MR sequence: comparison with MDCT. AJR Am J Roentgenol. 2005;185:979–984.

199.Seki S, Koyama H, Ohno Y, Nishio M, Takenaka D, Maniwa Y, et al. Diffusion-weighted MR imaging vs. multi-detector row CT: Direct comparison of capability for assessment of management needs for anterior mediastinal solitary tumors. Eur J Radiol. 2014;83(5): 835–842.

200.Sherry AD, Caravan P, Lenkinski RE. Primer on Gadolinium Chemistry. J. Magn. Reson. Imaging. 2009;30:1240–1248.

201.Sieren J, Ohno Y, Koyama H, Sugimura K, McLennan G.· Recent technological and application developments in computed tomography and magnetic resonance imaging for improved pulmonary nodule detection and lung cancer staging. J. Magn. Reson. Imaging. 2010;32:1353–1369.

202.Sileo C, Corvol H, Boelle PY, Blondiaux E, Clement A, Ducou, et al. HRCT and MRI of the lung in children with cystic fibrosis: comparison of different scoring systems. J Cyst Fibros. 2014;13(2):198-204.

203.Siltzbach LE. Effects of cortisone in sarcoidosis: a study of thirteen patients. Am J Med. 1952;12(2):139-160.

204.Simonetti OP, Finn JP, White RD, Laub G, Henry DA. “Black blood” T2-weighted inversion-recovery MR imaging of the heart. Radiology. 1996;199(1):49–57.

205.Simonetti OP, Kim RJ, Fieno DS, et al. An improved MR imaging technique for the visualization of myocardial infarction. Radiology 2001;218:215–223.

206.Sones M, Israel HL, Dratman MB, Frank JH. Effect of cortisone in sarcoidosis. N Engl J Med. 1951;244(6):209-213.

207.Souza CA, Muller NL, Flint J, Wright JL, Churg A. Idiopathic pulmonary fibrosis: spectrum of high-resolution CT findings. AJR Am J Roentgenol. 2005;185(6):1531–1539.

208.Spagnolo P, Sverzellati N, Wells AU, Hansell DM. Imaging aspects of the diagnosis of sarcoidosis. Eur Radiol. 2014;24:807–816.

209.Stein PD, Chenevert TL, Fowler SE, et al. Gadolinium-enhanced magnetic resonance angiography for pulmonary embolism: a multicenter prospective study (PIOPED III). Ann Intern Med. 2010;152:434–443.

210.Su S, Saunders JK, Smith IC. Resolving anatomical details in lung parenchyma: theory and experiment for a structurally and magnetically inhomogeneous lung imaging model. Magn Reson Med. 1995;33(6):760-5.

211.Tadamura et al. Effectiveness of Delayed Enhanced MRI for Identification of Cardiac Sarcoidosis: Comparison with Radionuclide Imaging. AJR 2005;185:110–115.

212.Takahashi K, Al-Janabi NJ. Computed tomography and magnetic resonance imaging of mediastinal tumors. J. Magn. Reson. Imaging. 2010;32:1325–1339.

213.Tawhai, M PhD, Ching-Long Lin PhD. Image-based modeling of lung structure and function. J. Magn. Reson. Imaging. 2010;32:1421–1431.

214.Theilmann RJ, Arai TJ, Samiee A, Dubowitz DJ, Hopkins SR, Buxton RB, Prisk GK. Quantitative MRI measurement of lung density must account for the change in T2* with lung inflation. J. Magn. Reson. Imaging. 2009;30:527–534.

215.Tokuda J, Schmitt M, Sun Y, Samuel Patz S, Yi Tang Y, Mountford CE, et al. Lung Motion and Volume Measurement by Dynamic 3D MRI Using a 128-Channel Receiver Coil. Acad Radiol. 2009;16(1):22–27.

216.Tremblay A Randomized Controlled Trial of Standard vs Endobronchial Ultrasonography-Guided Transbronchial Needle Aspiration in Patients With Suspected Sarcoidosis. CHEST 2009; 136: 340 –346.

217.Tsao J. Ultrafast Imaging: Principles, Pitfalls, Solutions, and Applications. J. Magn. Reson. Imaging. 2010;32:252–266.

218.Tustison, N, Brian B. Avants, Lucia Flors, Talissa A. Altes, Eduard E. de Lange, John P. Mugler III and James C. Gee. Ventilation-based segmentation of the lungs using hyperpolarized 3He MRI. J Magn Reson Imaging. 2011;34(4):831–841.

219.van Langevelde K, Tan M, Šrámek A, Huisman MV, de Roos A. Magnetic resonance imaging and computed tomography developments in imaging of venous thromboembolism. J. Magn. Reson. Imaging. 2010;32:1302–1312.

220.Verrecchia F, Mauviel A. Transforming growth factor-beta and fibrosis. World J. Gastroenterol. 2007 Jun;13(22):3056–3062.

221.Vogt FM, Herborn CU, Hunold P, et al. HASTE MRI versus chest radiography in the detection of pulmonary nodules: comparison with MDCT. AJR Am J Roentgenol. 2004; 183:71–78.

222.Watadani T, Sakai F, Johkoh T, et al. Interobserver variability in the CT assessment of honeycombing in the lungs. Radiology. 2013;266:936–944.

223.Wendland MF, Saeed M, Arheden H, et al . Toward necrotic cell fraction measurement by contrast-enhanced MRI of reperfused ischemically injured myocardium . Acad Radiol. 1998; 5(Suppl1):S42–S44.

224.Westbrook C, Kaut C. MRI in practice. 2nd edition, Blackwell, 1998.

225.Westbrook C. MRI at a glance. Blackwell Science, 2003.

226.Wielputz M. MRI of the lung: state of the art . Review. Diagn Interv Radiol. 2012;18:344–353.

227.Wu LM, Xu JR, Hua J, et al: Can diffusion-weighted imaging be used as a reliable sequence in the detection of malignant pulmonary nodules and masses? Magn Reson Imaging. 2013;31:235-246.

228.Wu LM, Xu JR, Gu HY, et al: Preoperative mediastinal and hilar nodal staging with diffusion-weighted magnetic resonance imaging and fluorodeoxyglucose positron emission tomography/computed tomography in patients with non–small-cell lung cancer: Which is better? J Surg Res. 2012;178:304-314.

229.Yarnykh VL, Yuan C. T1-insensitive flow suppression using quadruple inversion-recovery. Magn Reson Med. 2002;48(5):899-905.

230. Yi CA, Shin KM, Lee KS, Kim BT, Kim H, Kwon OJ, Choi JY, Chung MJ. Non-small cell lung cancer staging: efficacy comparison of integrated PET/CT versus 3.0-T whole-body MR imaging. Radiology. 2008;248(2):632-642.

231. Yi CA, Lee KS, Han J, Chung MP, Chung MJ, Shin KM. 3-T MRI for differentiating inflammation- and fibrosis-predominant lesions of usual and nonspecific interstitial pneumonia: comparison study with pathologic correlation. AJR Am J Roentgenol. 2008;190(4):878-885.

232. Yi CA, Shin KM, Lee KS, et al: Non–small cell lung cancer staging: Efficacy comparison of integrated PET/CT versus 3.0-T whole-body MR imaging. Radiology. 2008;248:632-642.

233. Yoon SH, Goo JM, Lee SM, et al: Positron emission tomography /magnetic resonance imaging evaluation of lung cancer: Current status and future prospects. J Thorac Imaging. 2014;29:4-16.

234. Zipse MM, Sauer WH. Cardiac sarcoidosis. Curr Cardiol Rep. 2014;16(8):514.

Appendix A

Bloch equations

If the magnetisation M is placed in a magnetic field B_0, then it experiences a torque T.

$T = M \times B_0$

This is because the cross product of two vectors is itself a vector, perpendicular to M and B_0, and its direction is given by the 'right hand rule' which describes the direction of magnet lines of flux and the cross product, knowing the direction of the original vectors.

Mathematically, the cross product can be quantified using determinants, and is equal to the area of the rectangle described by the original vectors.

Torque (T) is equal to the rate of change of the angular momentum (J) of the magnetic moment. (M)

$T = dJ/dt$

And as the angular momentum is related to the magnet moment by the gyromagnetic ratio (γ)

$J = 1/\gamma M$

then, $T = d/dt (1/\gamma M)$

thus, $dM/dt = \gamma T$

and $dM/dt = \gamma M \times B_0$

which is Bloch's equation, without the relaxation effects (of intra- and intermolecular phenomena).

So if:

$dM/dt = \gamma M \times B_0$

then

$d(M_x i + M_y j + M_z k) / dt = (M_x i + M_y j + M_z k) \times B_0 k$

If we use determinants to describe precession about B_0:

$dM/dt = \gamma M \times B_0$

$$= \gamma \begin{vmatrix} i & j & k \\ M_x & M_y & M_z \\ B_x & B_y & B_z \end{vmatrix}$$

as $B_x = 0$, $B_y = 0$

$$= \gamma \begin{vmatrix} i & j & k \\ M_x & M_y & M_z \\ 0 & 0 & B_0 \end{vmatrix}$$

$$= \gamma M_y B_0 i - \gamma M_x B_0 j$$

or taken in component form, equating the i, j and k terms;

$$dM_x / dt = \gamma M_y B_0$$

$$dM_y / dt = -\gamma M_x B_0$$

$$dM_z / dt = 0$$

Thus at time, t = 0, the component solutions, given - $B_0 \times \gamma = \omega_0$ (the precessional frequency):

$$Mx(t) = M_x(0) \cos(\omega_0 \times t) - M_y(0) \sin(\omega_0 \times t)$$

$$My(t) = M_x(0) \sin(\omega_0 \times t) + M_y(0) \cos(\omega_0 \times t)$$

$Mz\ (t) = 0$

Thus the Bloch equations can be solved at any t, to describe the magnetisation vector.

Now, in addition to the precessional motion, there are two relaxation effects, T^1 and. T^2, which ensure that the magnetisation return to thermal equilibrium by exponential decay.

If M_0 is the equilibrium magnetization along B_0 and M_z is the z-component under non-equilibrium conditions, then we assume that M_z approaches M_0 with first-order kinetics.

Thus:

$dM_z/dt = M_z - M_0/T^1$

whereT^1 is the spin lattice relaxation time.

And if M_0 is tilted off the z-axis by B_1, the individual spins will begin to precess at different rates due to spin-spin interactions, and local field inhomogeneities, and thus lose phase coherence. This effect is in the M_x and M_y planes only.

Thus:

$dM_x/dt = - M_x/T^2$

and

$dM_y/dt = - M_y/T^2$

where T^2 is the spin-spin relaxation time.

Appendix B

ST. GEORGE'S RESPIRATORY QUESTIONNAIRE (SGRQ)

This questionnaire is designed to help us learn much more about how your breathing is troubling you and how it affects your life. We are using it to find out which aspects of your illness cause you most problems, rather than what the doctors and nurses think your problems are.

Please read the instructions carefully and ask if you do not understand anything. Do not spend too long deciding about your answers.

Before completing the rest of the questionnaire:

Please tick in one box to show how you describe your current health:

Very good	☐
Good	☐
Fair	☐
Poor	☐
Very poor	☐

PART 1

Questions about how much chest trouble you have had over the past 3 months.

1. Over the past 3 months, I have coughed:

   most days a week ☐

   several days a week ☐

   a few days a month ☐

   only with chest infections ☐

   not at all ☐

2. Over the past 3 months, I have brought up phlegm (sputum):

   most days a week ☐

   several days a week ☐

   a few days a month ☐

   only with chest infections ☐

   not at all ☐

3. Over the past 3 months, I have had shortness of breath:

   most days a week ☐

   several days a week ☐

   a few days a month ☐

   only with chest infections ☐

   not at all ☐

4. Over the past 3 months, I have had attacks of wheezing:

most days a week ☐

several days a week ☐

a few days a month ☐

only with chest infections ☐

not at all ☐

5. During the past 3 months how many severe or very unpleasant attacks of chest trouble have you had?

more than 3 attacks ☐

3 attacks ☐

2 attacks ☐

1 attack ☐

no attacks ☐

6. How long did the worst attack of chest trouble last?
(Go to question 7 if you had no severe attacks)

a week or more ☐

3 or more days ☐

1 or 2 days ☐

less than a day ☐

not at all ☐

7. Over the past 3 months, in an average week, how many good days (with little chest trouble) have you had?

no good days ☐

1 or 2 good days ☐

3 or 4 good days ☐

nearly every day is good ☐

every day is good ☐

8. If you have a wheeze, is it worse in the morning?

no ☐

yes ☐

PART 2

Section 1

9. How would you describe your chest condition?

The most important problem i have ☐

Causes me quite a lot of problems ☐

Causes me a few problems ☐

Causes no problems ☐

10. If you have ever had paid employment.

My chest trouble made me stop work altogether □

My chest trouble interferes with my work or made me change my work □

My chest trouble does not affect my work □

Section 2

11. Questions about what activities usually make you feel breathless these days. Please tick (√) in each box that applies to you these days

	true	false
Sitting or lying still	□	□
Getting washed or dressed	□	□
Walking around the home	□	□
Walking outside on the level	□	□
Walking up a flight of stairs	□	□
Walking up hills	□	□
Playing sports or games	□	□

Section 3

12. Some more questions about your cough and breathlessness these days. Please tick (√) in each box that applies to you these days

	true	false

My cough hurts	□	□
My cough makes me tired	□	□
I am breathless when I talk	□	□
I am breathless when I bend over	□	□
My cough or breathing disturbs my sleep	□	□
I get exhausted easily	□	□

Section 4

13. Questions about other effects that your chest trouble may have on you these days.
Please tick (√) in each box that applies to you these days

	true	false
My cough or breathing is embarrassing in public	□	□
My chest trouble is a nuisance to my family, friends or neighbours	□	□
I get afraid or panic when I cannot get my breath	□	□
I feel that I am not in control of my chest problem	□	□
I do not expect my chest to get any better	□	□
I have become frail or an invalid because of my chest	□	□
Exercise is not safe for me	□	□
Everything seems too much of an effort	□	□

Section 5

14. Questions about your medication, if you are receiving no medication go straight to section 6. Please tick (√) in each box that applies to you these days

	true	false
My medication does not help me very much	□	□
I get embarrassed using my medication in public	□	□
I have unpleasant side effects from my medication	□	□
My medication interferes with my life a lot	□	□

Section 6

15. These are questions about how your activities might be affected by your breathing.
Please tick (√) in each box that applies to you because of your breathing

	true	false
I take a long time to get washed or dressed	□	□
I cannot take a bath or shower, or I take a long time	□	□
I walk slower than other people, or I stop for rests	□	□
Jobs like housework take a long time, or I have to stop for rests	□	□
If I walk up one flight of stairs, I have to go slowly or stop	□	□

If I hurry or walk fast, I have to stop or slow down □ □

My breathing makes it difficult to do things such as walk up hills, carrying things up stairs, light gardening such as weeding, dance,

play bowls or play golf □ □

My breathing makes it difficult to do things such as carry heavy loads, dig the garden or shovel snow, jog or walk at 5 miles per

hour, play tennis or swim □ □

My breathing makes it difficult to do things such as very heavy

manual work, run, cycle, swim fast or play competitive sports □ □

Section 7

16. We would like to know how your chest usually affects your daily life. Please tick (√) in each box that applies to you because of your chest trouble

true false

I cannot play sports or games □ □

I cannot go out for entertainment or recreation □ □

I cannot go out of the house to do the shopping □ □

I cannot do housework □ □

I cannot move far from my bed or chair □ □

17. Now would you tick in the box (one only) which you think best describes how your chest affects you:

It does not stop me doing anything I would like to do □

It stops me doing one or two things I would like to do □

It stops me doing most of the things I would like to do □

It stops me doing everything I would like to do □

Thank you for filling in this questionnaire. Before you finish would you please check to see that you have answered all the questions.